THE ASTROPHYSICAL JOURNAL, 495:196–221, 1998 March 1
© 1998. The American Astronomical Society. All rights reserved. Printed in U.S.A.

A NEAR-INFRARED IMAGING STUDY OF SEYFERT GALAXIES WITH EXTENDED EMISSION-LINE REGIONS

ALMUDENA ALONSO-HERRERO
Steward Observatory, University of Arizona, Tucson, AZ 85721
CHRIS SIMPSON[1]
Space Telescope Science Institute, 3700 San Martin Drive, Baltimore, MD 21218
MARTIN J. WARD
Department of Physics and Astronomy, University of Leicester, Leicester LE1 7RH, England
AND
ANDREW S. WILSON[2]
Astronomy Department, University of Maryland, College Park, MD 20742
Received 1997 May 30; accepted 1997 October 8

ABSTRACT

We present a near-infrared *J*-, *H*-, *K*-, and *L*′-band (1.25–3.80 μm) imaging study of a sample of Seyfert galaxies, including some of the best studied examples of those with extended emission-line regions (EELRs). The observed near-IR nuclear colors are consistent with a mixture of emissions from an old stellar population and unreddened hot dust. However, if the hot dust is located in the inner part of the dusty torus invoked in unified schemes, the dust emission should suffer substantial reddening. We show that the near-IR nuclear colors may also be reproduced with a combination of emission from unreddened starlight and hot ($T = 1200$ K) dust reddened by $A_V \approx 5$–30 mag. All of the galaxies exhibit an unresolved nuclear source at *L*′. The circumnuclear colors (in a 0.5–1.0 kpc annulus) are similar to those of normal spiral galaxies in most cases, although some galaxies exhibit extended emission at *L*′, presumably from hot dust, which causes the circumnuclear $K-L'$ colors to be redder than for normal galaxies. We argue that the circumnuclear hot dust in NGC 1068 and NGC 4151 is probably heated by young stars.

A detailed study of the morphologies of the central and circumnuclear regions of the galaxies in our sample is presented. We have constructed smooth models of the old stellar population by fitting elliptical isophotes to the *J*- and *K*-band images. The model-divided images are examined for the presence of isophotal deviations from elliptical symmetry, such as internal bars, spiral arms, etc., and compared with the structures seen in optical emission-line images, to study the relative orientations of bars, the EELRs, the nuclear radio emission, and the host galaxy. We find stellar bars in NGC 1068 and NGC 4253 whose orientations are consistent with those of their EELRs and evidence for double bars (or "bars within bars") in Mrk 573, NGC 3081, and NGC 3393. Only in NGC 2110 and NGC 4151 do we find no significant isophotal deviations from elliptical symmetry. Finally, there is an alignment on small scales between the near-IR continuum and the line emission in four galaxies, NGC 1068, NGC 2110, NGC 3081, and NGC 4253. These results seem to suggest that there is not a unique explanation for the orientation of the EELRs seen in Seyfert galaxies. In some cases, the EELRs could represent gas aligned with the nuclear stellar bars, whereas in others, they are more likely to be related to gas escaping along the minor axis of the galaxies.

Subject headings: galaxies: active — galaxies: nuclei — galaxies: photometry — galaxies: Seyfert — galaxies: stellar content — infrared: galaxies

1. INTRODUCTION

The unified model for active galactic nuclei (AGNs) explains the observed differences between certain types of AGNs in terms of an orientation dependence of some preferred axis with respect to the observer (see Antonucci 1993 for a recent review). The main observational evidence for such a scheme comes from spectropolarimetry, which reveals "hidden" broad-line regions (see, e.g., Antonucci & Miller 1985), and emission-line imaging, which shows elongated morphologies for the extended emission-line regions (EELRs) of many Seyfert 2 galaxies (see, e.g., Haniff, Wilson, & Ward 1988). In some cases, the emission-line images exhibit striking conical or biconical structures (e.g., NGC 5252—Tadhunter & Tsvetanov 1989; NGC 5728—Wilson et al. 1993; and NGC 5643—Simpson et al. 1997). These "ionization cones" can be traced down to a few tens of parsecs from the nucleus (e.g., NGC 1068—Evans et al. 1991; NGC 4151—Evans et al. 1993), and the cone axis is generally aligned with that of the radio ejecta to within a few degrees (Wilson & Tsvetanov 1994).

In the unified scheme, these observations are usually explained by an optically thick torus that surrounds the nuclear engine and the broad-line region, which obscures them from view in Seyfert 2 galaxies. This torus is also able to collimate the radiation and produce the conical emission-line structures. Although this is an appealing model, there is currently little direct evidence for the exis-

[1] Present address: Jet Propulsion Laboratory, 4800 Oak Grove Drive, Pasadena, CA 91109.
[2] Adjunct Astronomer, Space Telescope Science Institute, 3700 San Martin Drive, Baltimore, MD 21218.

tence of the torus itself, and different physical sizes and geometries have been proposed for the obscuring torus. Hot dust ($T = 1000$–1300 K) has been found to make an important contribution to the near-infrared (near-IR) emission from the centers of Seyfert galaxies (Glass & Moorwood 1985; Kotilainen et al. 1992b; Alonso-Herrero, Ward, & Kotilainen 1996b), and it is natural to consider the possibility that this dust lies within the torus. If the dust in the inner walls of the torus has a temperature $T \simeq 10^3$ K, then the inner edge of the torus must only be a few parsecs from the nuclear continuum source (Krolik & Begelman 1988; Lawrence 1991), in good agreement with the models of the spectral energy distribution of NGC 1068 (Pier & Krolik 1993). The total extent of the torus, however, may be much greater, perhaps several hundred parsecs. Granato & Danese (1994) have fitted the spectral distribution energies of a sample of Seyfert galaxies with optically thick tori with ratios of the outer to the inner radius $3 \leq r_o/r_i \leq 3000$. Using more indirect arguments based on the relative numbers of Seyfert 1, intermediate, and Seyfert 2 galaxies, Maiolino & Rieke (1995) and McLeod & Rieke (1995) have suggested that the last two kinds of Seyfert galaxies are Seyfert 1 galaxies seen through a 100 pc inner radius torus coplanar with the galactic disk plane. Although there are few direct observational constraints on the geometry of the torus, high-resolution imaging has revealed structure in the centers of Seyfert galaxies that supports the torus picture. Red features have been found in color maps (see, e.g., Kotilainen & Prieto 1995; Simpson et al. 1996), and dust lanes have been observed in *Hubble Space Telescope* (*HST*) images (see, e.g., NGC 5728—Wilson et al. 1993; NGC 5643—Simpson et al. 1997), in all cases straddling the nucleus and oriented perpendicular to the radio/EELR axis. Although the resolution of these images is far larger than the scale of the inner radius of the torus, they indicate that dust has settled in the equatorial plane and that these structures may be dynamically linked with the torus proper.

In this paper, we present near-IR imaging observations (from 1.25 to 3.80 μm) of a sample of Seyfert galaxies, many of which possess EELRs. This study was designed to carry out a detailed analysis of the innermost 0.5 and 1 kpc, as well as the larger scale structures of the galaxies. Smooth galaxy models are constructed by fitting elliptical isophotes, examined for isophotal deviations from elliptical symmetry, and compared with the morphology of the EELRs, in order to test whether there is any relationship between the EELRs and the circumnuclear regions when observed in the near-IR. The paper is organized as follows. In § 2, we describe the observations and their reduction. Section 3 discusses the $\simeq 1$ kpc scale colors of the sample of Seyfert galaxies and describes their L'-band properties and the morphologies of their central and circumnuclear regions. The results are discussed in § 4. Conclusions are summarized in § 5.

2. OBSERVATIONS

We have obtained near-IR imaging of a sample of 12 Seyfert galaxies through J ($\lambda_c = 1.25$ μm), H ($\lambda_c = 1.65$ μm), K ($\lambda_c = 2.20$ μm), and L' ($\lambda_c = 3.80$ μm) filters. The Seyfert galaxies were selected according to the criterion that they show ionization cones or EELRs in [O III] λ5007 and/or Hα + [N II] images. The sample, which is not complete, is composed of type 1.5–2 Seyfert galaxies, which includes some of the brightest and best studied examples of their class. The observations were carried out with the IR camera IRCAM3 on the 3.9 m United Kingdom Infrared Telescope (UKIRT) during two observing runs, 1995 January 2–5 and 1996 December 30, with pixel sizes 0.″286 pixel^{-1} and 0.″143 pixel^{-1}, respectively. The size of the J, H, and K images is 256×256 pixels, whereas the size of the L' images is 64×64 pixels. In some frames taken on the 1995 January run, wind shake produced an artificial east-west elongation of the images; the shape of the images in the inner few arcseconds should be treated with caution. For this reason, new images of seven galaxies were obtained in the 1996 December run with a smaller pixel size and using a rapid guider, which greatly reduces the effects of wind shake and improves the image quality. Conditions in the 1996 December run were nonphotometric. The sample is presented in Table 1, where the last column indicates the observing runs and filters in which the galaxy was observed.

The observational procedure involved taking several images of the galaxy that were alternated with adjacent blank areas of sky with the same number of co-adds and on-source integration times. The sky images were used for

TABLE 1

THE SAMPLE

Galaxy	R.A. (B1950)	Decl. (B1950)	v_{hel} (km s^{-1})	Class	Morphological Type	Run (Filters)
Mrk 348	00 46 04.9	+31 41 04.1	4540	Sy 2	SA(s)0/a	1995 Jan (*JHKL*)
Mrk 573	01 41 22.9	+02 05 56.3	5174	Sy 2	(R)SAB(rs)0	1995 Jan (*JHKL*)
NGC 1068	02 40 07.1	−00 13 31.5	1136	Sy 2	(R)SA(rs)b	1995 Jan (*JHKL*)
NGC 2110	05 49 46.4	−07 28 01.9	2284	Sy 2	SAB0	1995 Jan (*JHKL*), 1996 Dec (*JHK*)
NGC 2992	09 43 17.7	−14 05 42.8	2314	Sy 2	Sa pec	1995 Jan (*JHKL*), 1996 Dec (*JHK*)
NGC 3081	09 57 10.0	−22 35 10.2	2394	Sy 2	(R_1)SAB(r)0/a	1995 Jan (*JHKL*), 1996 Dec (*JHK*)
NGC 3393	10 46 00.0	−24 53 48.0	4107	Sy 2	(R)SB(s)ab	1995 Jan (*JHK*), 1996 Dec (*JHK*)
NGC 4151	12 08 01.1	+39 41 01.8	1281	Sy 1.5	(R′)SAB(rs)ab	1995 Jan (*JHKL*)
NGC 4253	12 15 55.6	+30 05 25.6	3876	Sy 1.5	(R′)SB(s)a	1995 Jan (*JHK*), 1996 Dec (*JHK*)
NGC 4388[a]	12 23 14.6	+12 56 17.4	2524	Sy 2	SA(s)b	1995 Jan (*JHKL*), 1996 Dec (*JHK*)
NGC 5252	13 35 44.4	+04 47 47.1	6890	Sy 1.9	S0	1995 Jan (*JHKL*), 1996 Dec (*JK*)
Mrk 463W	13 53 39.6	+18 36 56.5	15113	...	...	1995 Jan (*JHKL*)
Mrk 463E	13 53 39.9	+18 36 57.9	15113	Sy 1.9	...	1995 Jan (*JHKL*)

NOTES.—Equatorial coordinates, velocities, Seyfert class, and morphological types have been obtained from NASA/IPAC Extragalactic Database (NED). Units of right ascension are hours, minutes, and seconds, and units of declination are degrees, arcminutes, and arcseconds.

[a] Throughout this paper NGC 4388 is assumed to be located at the distance of the Virgo Cluster (see, e.g., Stone, Wilson, & Ward 1988), $d = 17.1$ Mpc (Freedman et al. 1994).

both flat-fielding and sky background subtraction. The individual object frames were offset a few arcseconds so that residual pixel-to-pixel sensitivity variations and the effects of bad pixels were minimized. Standard reduction procedures, involving dark-current subtraction, flat-field correction, bad pixel removal, background subtraction, and individual galaxy image registration, were used.

Conditions were photometric during the 1995 January run so standard star observations were used to perform the photometric calibration of the images. A number of standard stars taken from the list given in Elias et al. (1982) were observed several times throughout each night and reduced in a similar way. A flux calibration solution for each filter was calculated for the entire set of standard star observations, as no systematic variations were found between different nights. The calibration was determined using a three-parameter regression (zero point, extinction coefficient, and color term). The major source of uncertainty in near-IR observations comes from the background subtraction. The size of the J, H, and K 1995 January images is large enough that most of the galaxies do not fill the detector field of view, which allows us to measure the residual sky level uncertainties in blank areas. These uncertainties were found to be less than 0.5% of the original sky background, and no systematic positive residuals are present, which indicates that in most cases, the galaxy light does not fill the image. In the case of the L'-band imaging, we find that the majority of the galaxies are compact, which again allows us to quantify the uncertainties associated with the background subtraction in blank areas on the edges of the images. Because of the higher variability of the sky at this wavelength, the uncertainties tend to be larger, 2%–3% of the original sky value. Typical errors from the photometric calibration are 0.09, 0.04, 0.08, and 0.04 mag in J, H, K, and L', respectively. Since the observing conditions during the 1996 December run were nonphotometric, the magnitudes from the 1995 January observations were used to flux-calibrate the images by means of multiple-aperture photometry. Owing to the smaller pixel size of the 1996 December observations, we were able to measure magnitudes and colors for a 1.″5 diameter aperture, with errors typically between 5% and 10% (owing to the uncertainties on the sky background value). The full width half-maximum (FWHM) was measured from the standard stars and stars on the galaxy frames as 1″–1.″2 and 0.″7–1″ at K band for the 1995 January and 1996 December runs, respectively.

Standard synthetic aperture photometry was performed on all the 1995 January near-IR images using the IRAF APPHOT routines. Circular apertures were used to obtain magnitudes for each object. The magnitudes were measured

TABLE 2

SYNTHETIC APERTURE NEAR-IR PHOTOMETRY

Galaxy (1)	t_{int} (s) (2)	Aperture Diameter (arcsec) (3)	$J-H$ (4)	$H-K$ (5)	$K-L'$ (6)	K (7)
Mrk 348	J 360	3	0.80	0.55	1.67	12.17
	H 360	6	0.75	0.44	...	11.62
	K 360	9	0.73	0.42	...	11.31
	L' 1055	12	0.71	0.43	...	11.09
		15	0.70	0.44	...	10.93
Mrk 573	J 360	3	0.68	0.49	1.64	11.78
	H 360	6	0.68	0.40	1.24	11.18
	K 360	9	0.66	0.37	...	10.93
	L' 1176	12	0.66	0.36	...	10.76
		15	0.66	0.35	...	10.63
		30	0.64	0.35	...	10.29
NGC 1068.....	J 360	3	1.15	1.10	3.70	8.11
	H 360	6	1.00	0.88	3.36	7.65
	K 360	9	0.92	0.75	3.10	7.36
	L' 543	12	0.86	0.68	2.93	7.16
		15	0.85	0.61	...	7.00
		30	0.80	0.48	...	6.50
NGC 2110.....	J 360 (360)	1.5	0.93	1.00	...	11.37
	H 360 (300)	3	0.84	0.76	1.52	10.60
	K 360 (300)	6	0.85	0.54	1.10	9.86
	L' 1176	9	0.84	0.47	...	9.48
		12	0.84	0.42	...	9.24
		15	0.84	0.40	...	9.06
		30	0.84	0.33	...	8.61
NGC 2992.....	J 360 (360)	1.5	0.84	0.55	...	12.02
	H 360 (300)	3	0.80	0.61	0.96	10.95
	K 360 (300)	6	0.83	0.51	0.73	10.19
	L' 1176	9	0.83	0.47	0.66	9.82
		12	0.82	0.45	...	9.58
		15	0.81	0.44	...	9.41
		30	0.78	0.42	...	8.92
NGC 3081.....	J 300 (360)	1.5	0.74	0.39	...	12.83
	H 300 (300)	3	0.72	0.32	0.93	11.79
	K 300 (300)	6	0.66	0.28	0.56	10.89
	L' 1176	9	0.65	0.25	...	10.45
		12	0.63	0.25	...	10.14
		15	0.63	0.23	...	9.96
		30	0.62	0.20	...	9.59

TABLE 2—*Continued*

Galaxy (1)	t_{int} (s) (2)	Aperture Diameter (arcsec) (3)	$J-H$ (4)	$H-K$ (5)	$K-L'$ (6)	K (7)
NGC 3393.....	*J* 360 (360)	1.5	0.76	0.24	...	12.60
	H 360 (300)	3	0.66	0.29	...	11.51
	K 360 (300)	6	0.66	0.26	...	10.77
		9	0.64	0.26	...	10.45
		12	0.64	0.26	...	10.23
		15	0.64	0.25	...	10.07
		30	0.60	0.24	...	9.64
NGC 4151.....	*J* 360	3	0.97	0.93	1.88	8.66
	H 360	6	0.90	0.83	1.81	8.45
	K 360	9	0.86	0.77	1.81	8.33
	L' 543	12	0.83	0.73	...	8.24
		15	0.81	0.69	...	8.17
		30	0.73	0.62	...	7.90
NGC 4253.....	*J* 300 (360)	1.5	1.13	1.12	...	10.74
	H 300 (300)	3	1.02	1.03	...	10.40
	K 300 (300)	6	0.91	0.93	...	10.13
		9	0.85	0.87	...	10.01
		12	0.80	0.82	...	9.93
		15	0.77	0.78	...	9.86
		30	0.67	0.69	...	9.65
NGC 4388.....	*J* 360 (360)	1.5	1.11	0.90	...	12.21
	H 360 (300)	3	1.02	0.68	1.94	11.46
	K 360 (300)	6	0.94	0.52	1.45	10.77
	L' 543	9	0.89	0.45	...	10.36
		12	0.85	0.40	...	10.07
		15	0.82	0.37	...	9.84
		30	0.76	0.29	...	9.16
NGC 5252.....	*J* 300 (360)	1.5	1.47[a]	...	...	12.80
	H 300	3	0.71	0.53	1.45	12.03
	K 300 (300)	6	0.69	0.41	...	11.32
	L' 693	9	0.68	0.36	...	10.96
		12	0.67	0.34	...	10.72
		15	0.67	0.32	...	10.55
		30	0.67	0.30	...	10.10
Mrk 463 E	*J* 360	2	1.72	1.68	2.56	10.86
	H 360	4	1.57	1.60	2.29	10.39
Mrk 463 W.....	*K* 360	2	0.72	0.46	...	13.77
	L' 211	4	0.74	0.50	...	12.82

NOTE.—The mean sky surface brightnesses are μ_J(sky) = 15.77 ± 0.30 mag arcsec^{-2}, μ_H(sky) = 14.15 ± 0.40 mag arcsec^{-2}, μ_K(sky) = 12.89 ± 0.12 mag arcsec^{-2}, and $\mu_{L'}$(sky) = 3.41 ± 0.05 mag arcsec^{-2}.

[a] $J-K$ color.

through 3″, 6″, 9″, 12″, 15″, and 30″ (when possible) diameter apertures in the *J*, *H*, and *K* images, and 3″ and 6″ (when possible) diameter apertures in the *L'*-band images (1995 January data). Note that in the case of Mrk 463E+W, 2″ and 4″ diameter apertures were used to allow us to get measurements for both nuclei. As noted above, when 1.″5 diameter aperture photometry is given, the data correspond to the 1996 December run. Good agreement (to within 20%) is found when comparing our results with previously published aperture photometry (Glass & Moorwood 1985; Boisson & Durret 1986; Kotilainen et al. 1992a; McLeod & Rieke 1995; Alonso-Herrero et al. 1996b). At the bottom of Table 2 we list the average sky brightness of the sky for each filter as measured from the images taken on the 1995 January run.

3. RESULTS

The aperture photometry is presented in Table 2, in which column (2) gives the integration times in seconds for each filter for the 1995 January data and, enclosed in parentheses, for those galaxies observed on 1996 December. Columns (4)–(7) are the $J-H$, $H-K$, and $K-L'$ colors and the *K*-band magnitude, respectively. Contour plots on a logarithmic scale of the 256 × 256 pixel *J*- (the *H*- and *K*-band images show similar morphologies) and 64 × 64 pixel *L'*-band images (1995 January data) are presented in Figure 1. The *L'*-band images have been plotted on the same scale as the *J*-band images to allow a direct comparison of sizes and orientations in the nuclear regions. At the top of the *L'*-band panel of each galaxy, the linear size corresponding to 10″ has been indicated (at the distances calculated from the heliocentric velocities listed in Table 1, assuming $H_0 = 50$ km s^{-1} Mpc^{-1}). It is clear from this figure that in most cases the *L'*-band emission is confined to the nuclear regions with, at most, a small contribution from the underlying galaxy. This point will discussed in more detail in § 3.2.

3.1. *The Near-IR Colors of the Central and Circumnuclear Regions*

Previous studies of the near-IR continuum of Seyfert galaxies (Glass & Moorwood 1985; Kotilainen et al. 1992b; Alonso-Herrero et al. 1996b) concluded that their $J-H$, $H-K$, and $K-L$ nuclear colors can be explained by a model involving a normal stellar component plus a hot dust component in emission. Alonso-Herrero et al. (1996b) also showed that the $K-L$ color is more sensitive to the pres-

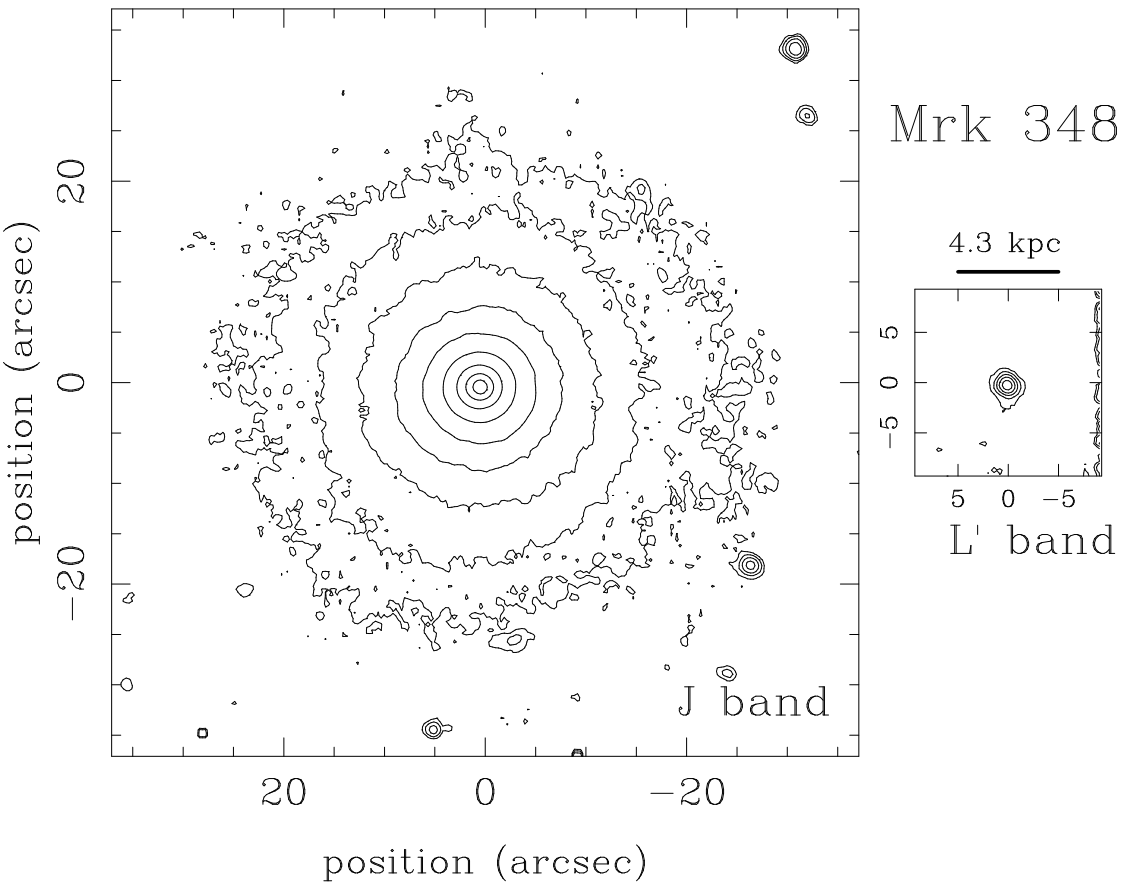

FIG. 1*a*

FIG. 1.—(*a*) Mrk 348. Contour plots on a logarithmic scale of the *J*- and *L'*-band images of the sample of Seyfert galaxies observed during the 1995 January run. North is up, and east is to the left. Note that the 64 × 64 pixel *L'*-band images have been plotted at the same scale as the *J*-band images. The lowest level displayed in the *J*-band contour plot is 21.39 mag arcsec^{-2}, and successive contours are separated by 0.75 mag arcsec^{-2}. The lowest level displayed in the *L'*-band contour plot is 14.62 mag arcsec^{-2}, and successive contours are separated by 0.75 mag arcsec^{-2}. (*b*) Mrk 573. The lowest level displayed in the *J*-band contour plot is 21.29 mag arcsec^{-2}, and successive contours are separated by 0.75 mag arcsec^{-2}. The lowest level displayed in the *L'*-band contour plot is 14.86 mag arcsec^{-2}, and successive contours are separated by 0.75 mag arcsec^{-2}. (*c*) NGC 1068. The lowest level displayed in the *J*-band contour plot is 17.18 mag arcsec^{-2}, and successive contours are separated by 0.40 mag arcsec^{-2}. The lowest level displayed in the *L'*-band contour plot is 13.08 mag arcsec^{-2}, and successive contours are separated by 0.75 mag arcsec^{-2}. (*d*) NGC 2110. The lowest level displayed in the *J*-band contour plot is 19.95 mag arcsec^{-2}, and successive contours are separated by 0.50 mag arcsec^{-2}. The lowest level displayed in the *L'*-band contour plot is 14.10 mag arcsec^{-2}, and successive contours are separated by 0.60 mag arcsec^{-2}. (*e*) NGC 2992. The lowest level displayed in the *J*-band contour plot is 20.38 mag arcsec^{-2}, and successive contours are separated by 0.50 mag arcsec^{-2}. The lowest level displayed in the *L'*-band contour plot is 14.76 mag arcsec^{-2}, and successive contours are separated by 0.50 mag arcsec^{-2}. (*f*) NGC 3081. The lowest level displayed in the *J*-band contour plot is 19.53 mag arcsec^{-2}, and successive contours are separated by 0.40 mag arcsec^{-2}. The lowest level displayed in the *L'*-band contour plot is 15.15 mag arcsec^{-2}, and successive contours are separated by 0.40 mag arcsec^{-2}. (*g*) NGC 3393. The lowest level displayed in the *J*-band contour plot is 20.21 mag arcsec^{-2}, and successive contours are separated by 0.60 mag arcsec^{-2}. (*h*) NGC 4151. The lowest level displayed in the *J*-band contour plot is 18.72 mag arcsec^{-2}, and successive contours are separated by 0.50 mag arcsec^{-2}. The lowest level displayed in the *L'*-band contour plot is 12.96 mag arcsec^{-2}, and successive contours are separated by 0.75 mag arcsec^{-2}. (*i*) NGC 4253. The lowest level displayed in the *J*-band contour plot is 19.10 mag arcsec^{-2}, and successive contours are separated by 0.60 mag arcsec^{-2}. (*j*) NGC 4388. The lowest level displayed in the *J*-band contour plot is 20.88 mag arcsec^{-2}, and successive contours are separated by 0.50 mag arcsec^{-2}. The lowest level displayed in the *L'*-band contour plot is 14.91 mag arcsec^{-2}, and successive contours are separated by 0.50 mag arcsec^{-2}. (*k*) NGC 5252. The lowest level displayed in the *J*-band contour plot is 21.16 mag arcsec^{-2}, and successive contours are separated by 0.60 mag arcsec^{-2}. The lowest level displayed in the *L'*-band contour plot is 14.55 mag arcsec^{-2}, and successive contours are separated by 0.75 mag arcsec^{-2}. (*l*) Mrk 463E + W. The lowest level displayed in the *J*-band contour plot is 21.72 mag arcsec^{-2}, and successive contours are separated by 0.60 mag arcsec^{-2}. The lowest level displayed in the *L'*-band contour plot is 14.17 mag arcsec^{-2}, and successive contours are separated by 0.75 mag arcsec^{-2}.

ence of hot dust and less affected by extinction than other near-IR or optical colors. This study, however, suffered from a lack of sensitive small-aperture *L*-band ($\lambda_c = 3.4$ μm) measurements, since only a few galaxies were imaged in this filter. The present study offers a number of advantages. First, a smaller pixel size was used to obtain more reliable small-aperture measurements. Second, both the good photometric and seeing conditions during the 1995 January run allowed us to produce more accurate magnitudes and colors (note that approximately 50% of the observations in Alonso-Herrero et al. 1996b had to be calibrated with previously published photometry). Third, good quality *L'*-band imaging data were obtained for most of the galaxies in our sample.

In addition to the colors measured with a given angular size (Table 2), we have computed near-IR colors from regions with a given linear size (Table 3). The minimum projected aperture diameter is determined by the spatial resolution of the images and the galaxy distances, and we chose two apertures with projected diameters of 0.5 and 1

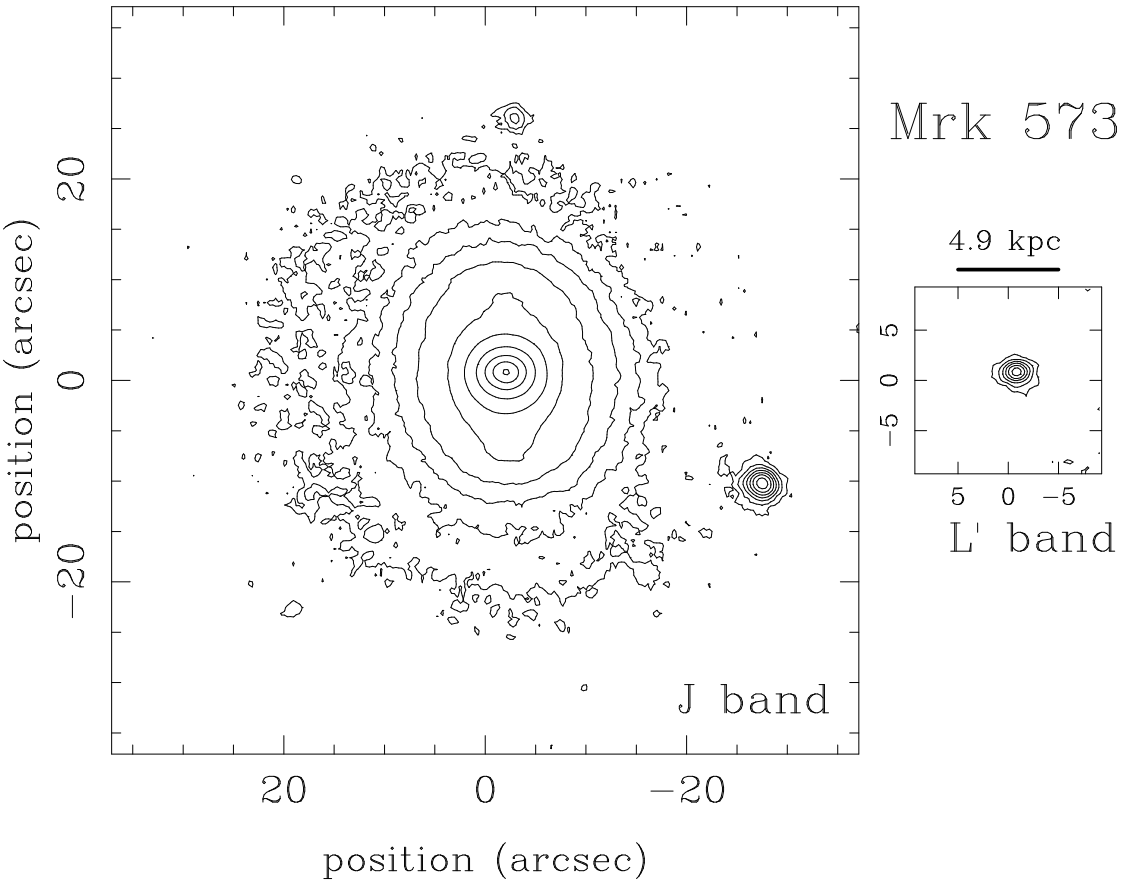
Mrk 573
4.9 kpc
J band
L' band
position (arcsec)
position (arcsec)
20
0
−20
5
0
−5

FIG. 1*b*

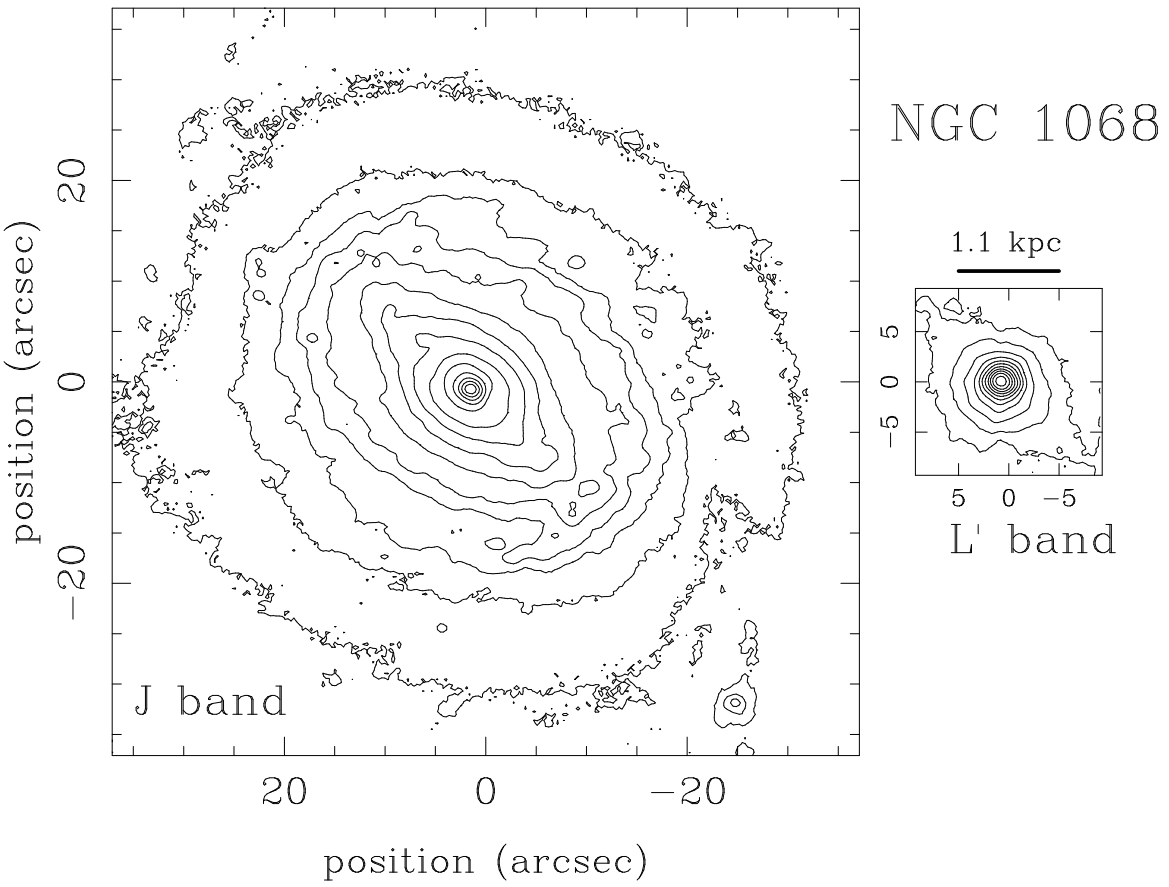
NGC 1068
1.1 kpc
J band
L' band
position (arcsec)
position (arcsec)
20
0
−20
5
0
−5

FIG. 1*c*

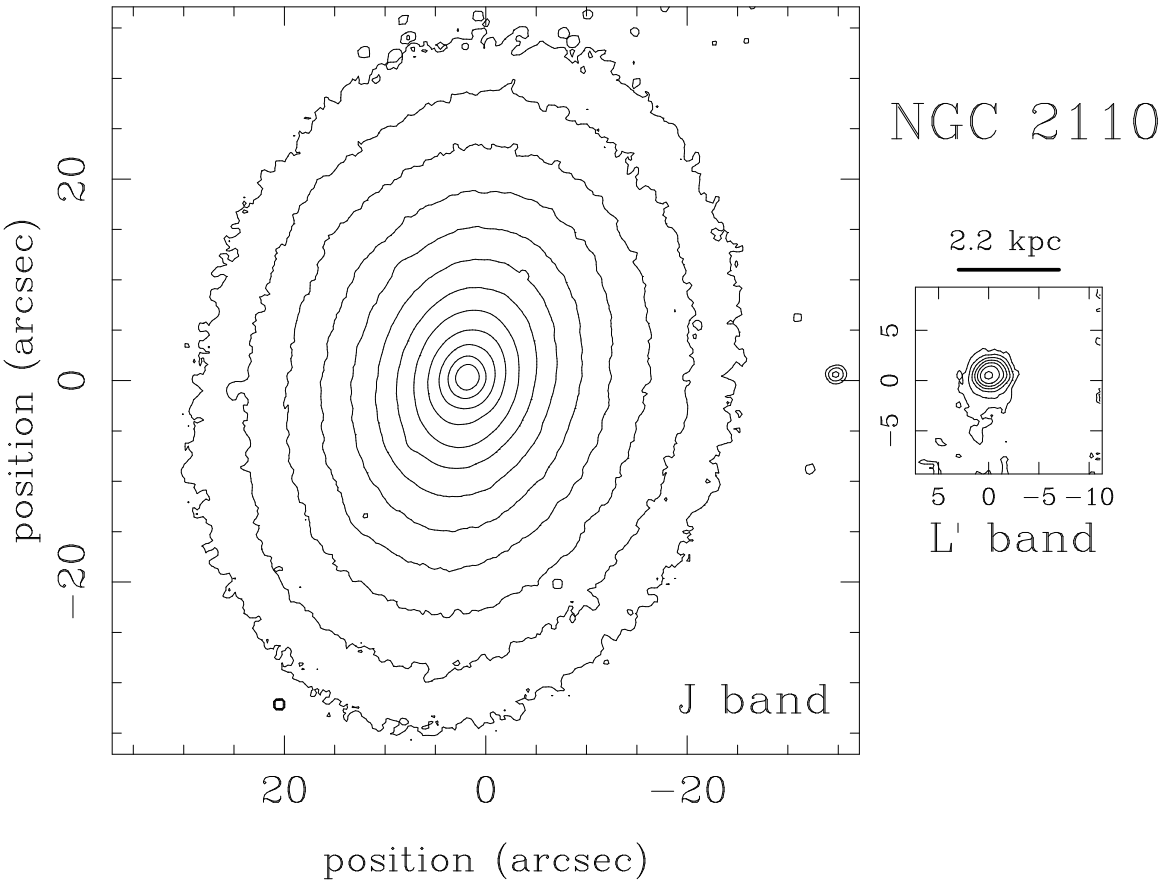
NGC 2110
2.2 kpc
J band
L' band
position (arcsec)
position (arcsec)
20
0
−20
5
0
−5
−10

FIG. 1*d*

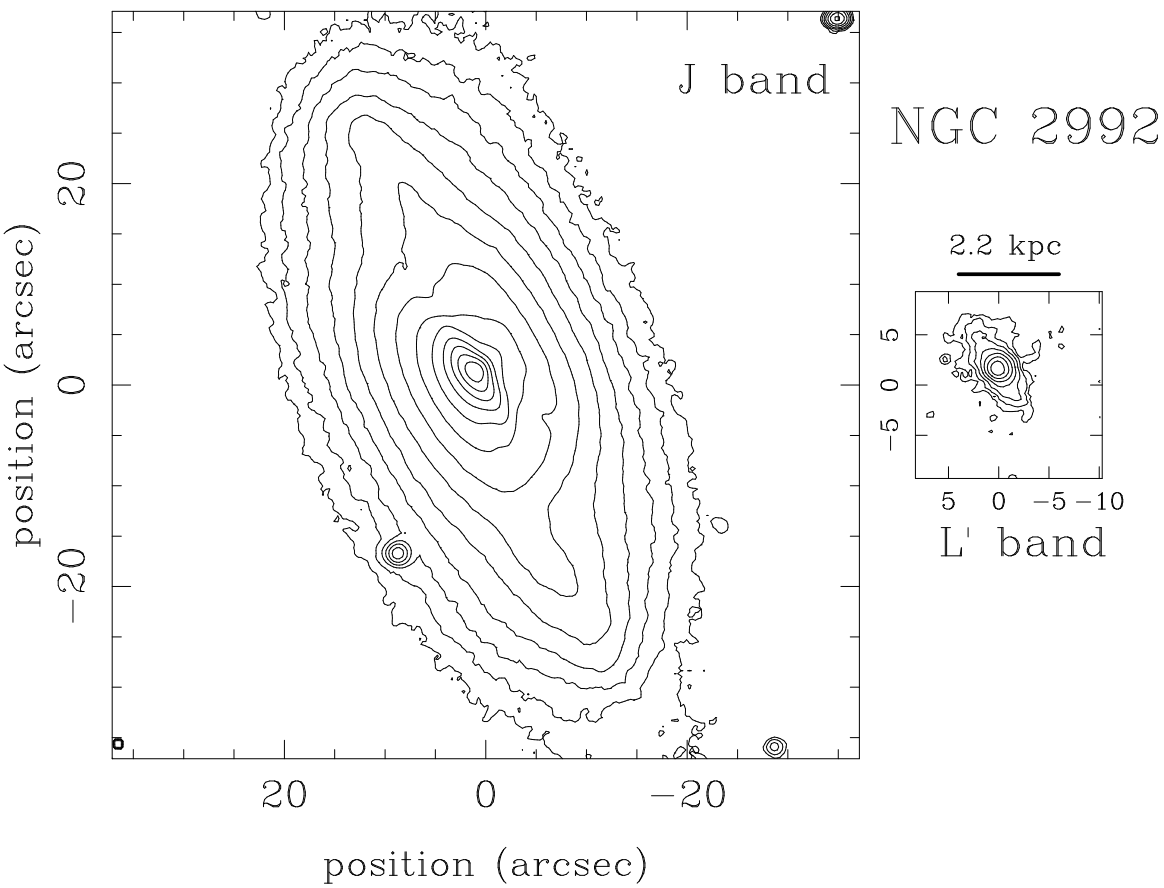
NGC 2992
2.2 kpc
J band
L' band
position (arcsec)
position (arcsec)
20
0
−20
5
0
−5
−10

FIG. 1*e*

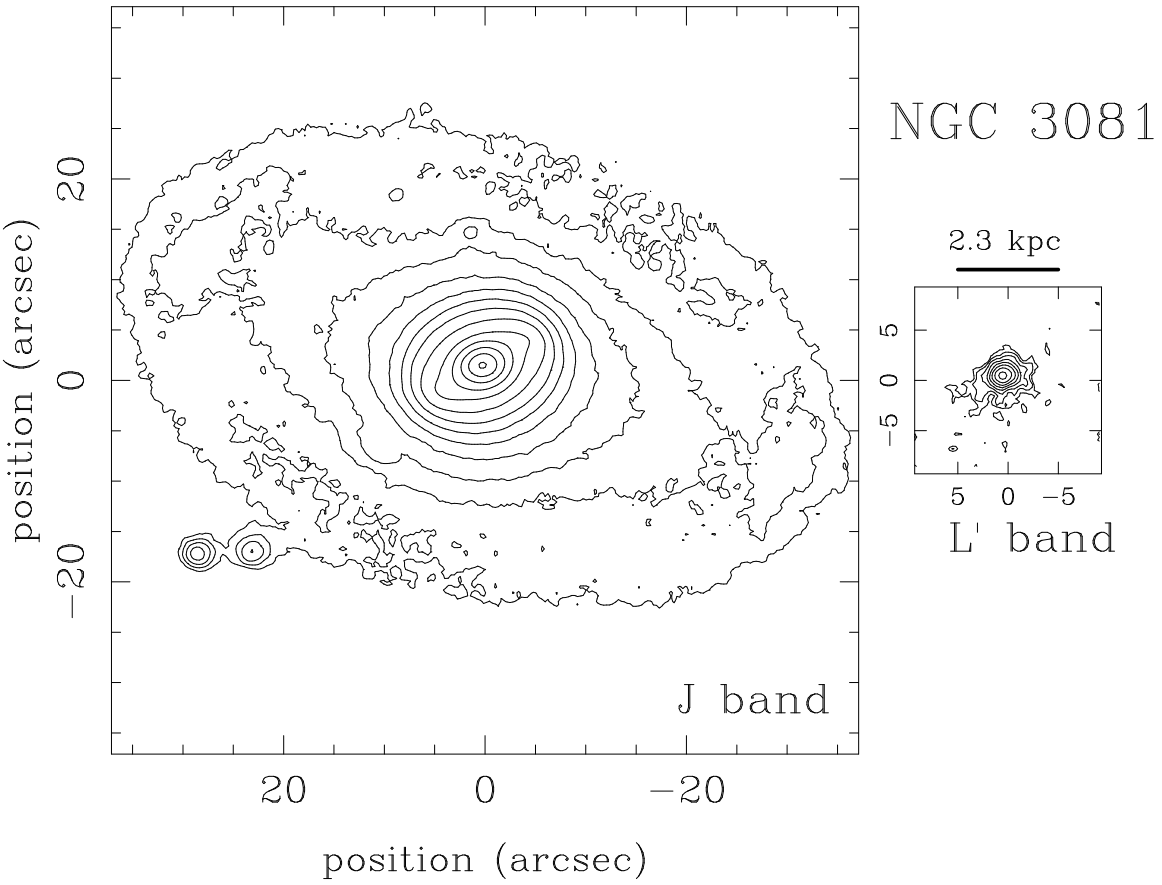
NGC 3081
2.3 kpc
J band
L' band
position (arcsec)
position (arcsec)
20
0
−20
5
0
−5

FIG. 1*f*

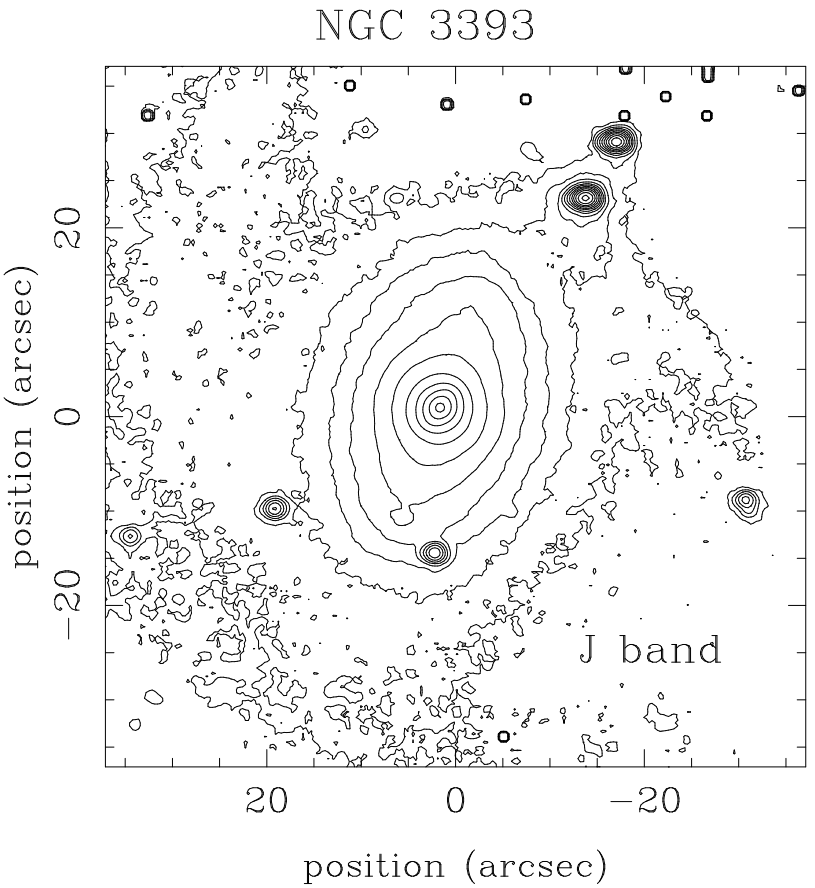
NGC 3393
J band
position (arcsec)
position (arcsec)
20
0
−20

FIG. 1*g*

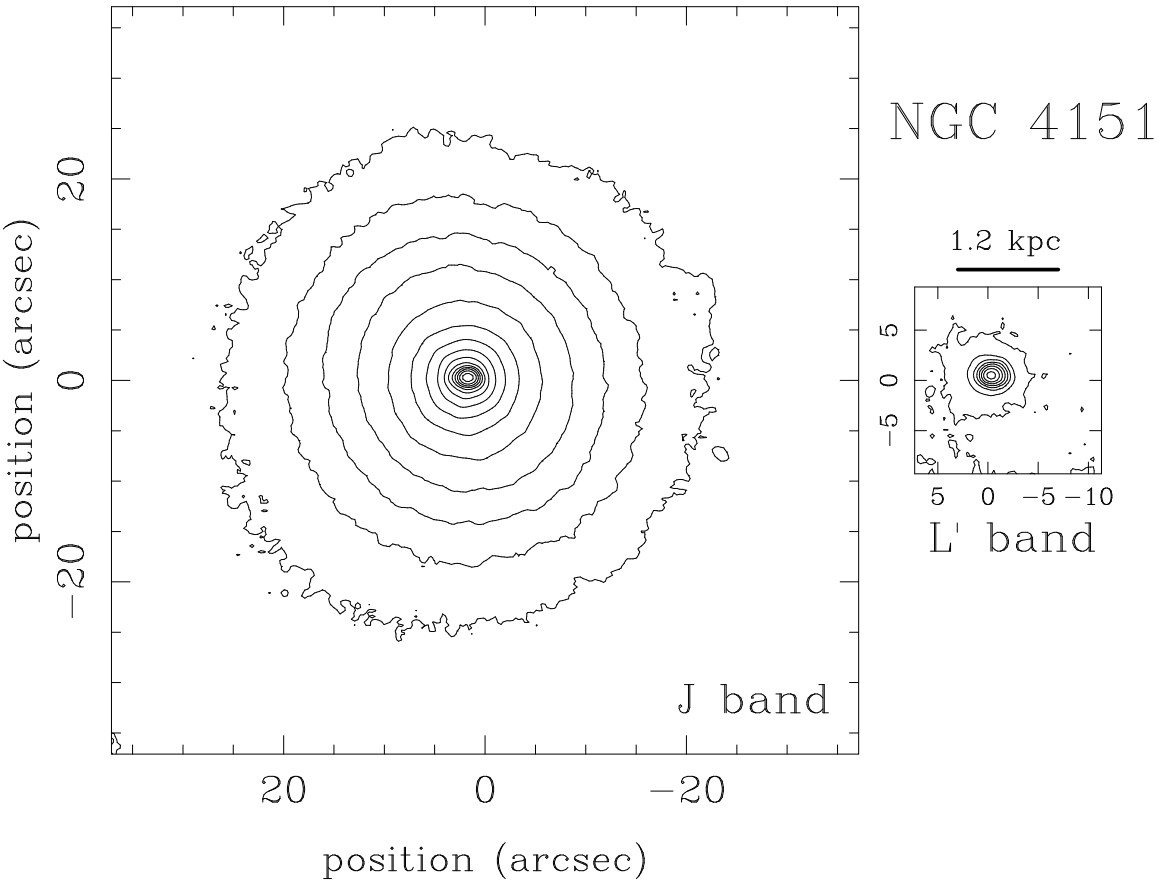
NGC 4151
1.2 kpc
J band
L' band
position (arcsec)
position (arcsec)
20
0
−20
5
0
−5
−10

FIG. 1*h*

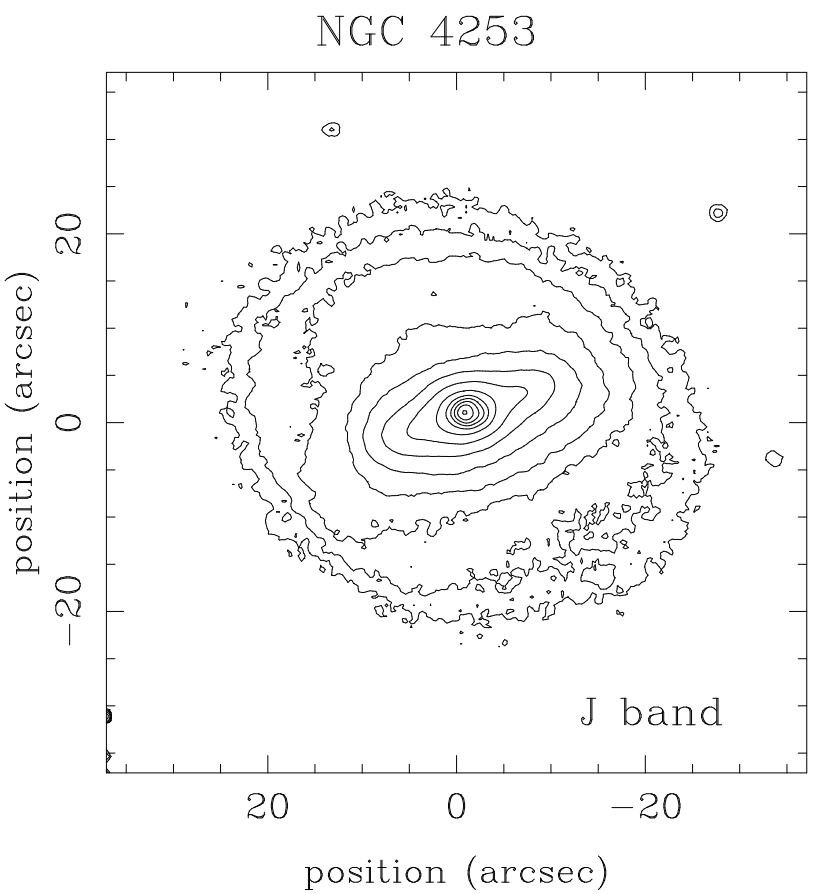
NGC 4253
J band
position (arcsec)
position (arcsec)
20
0
−20

FIG. 1*i*

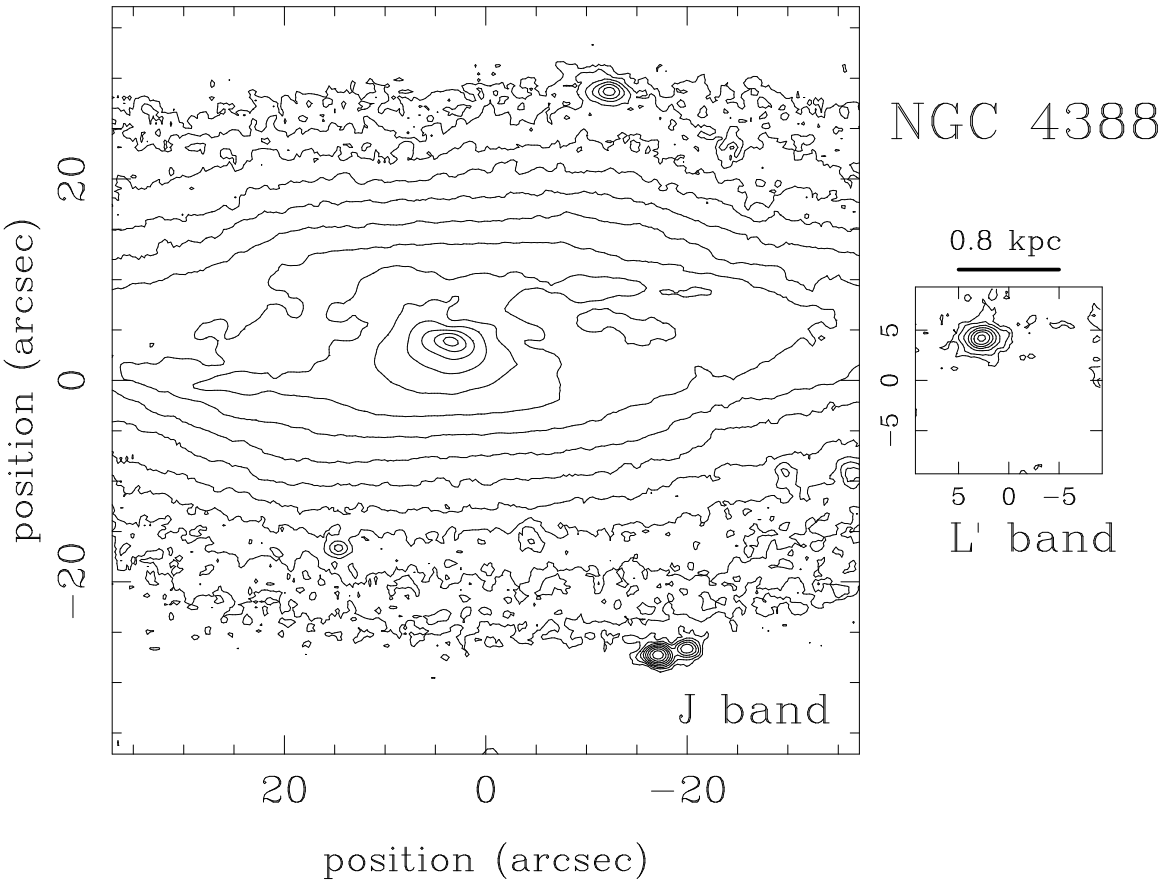
NGC 4388
0.8 kpc
J band
L' band
position (arcsec)
position (arcsec)
20
0
−20
5
0
−5

FIG. 1*j*

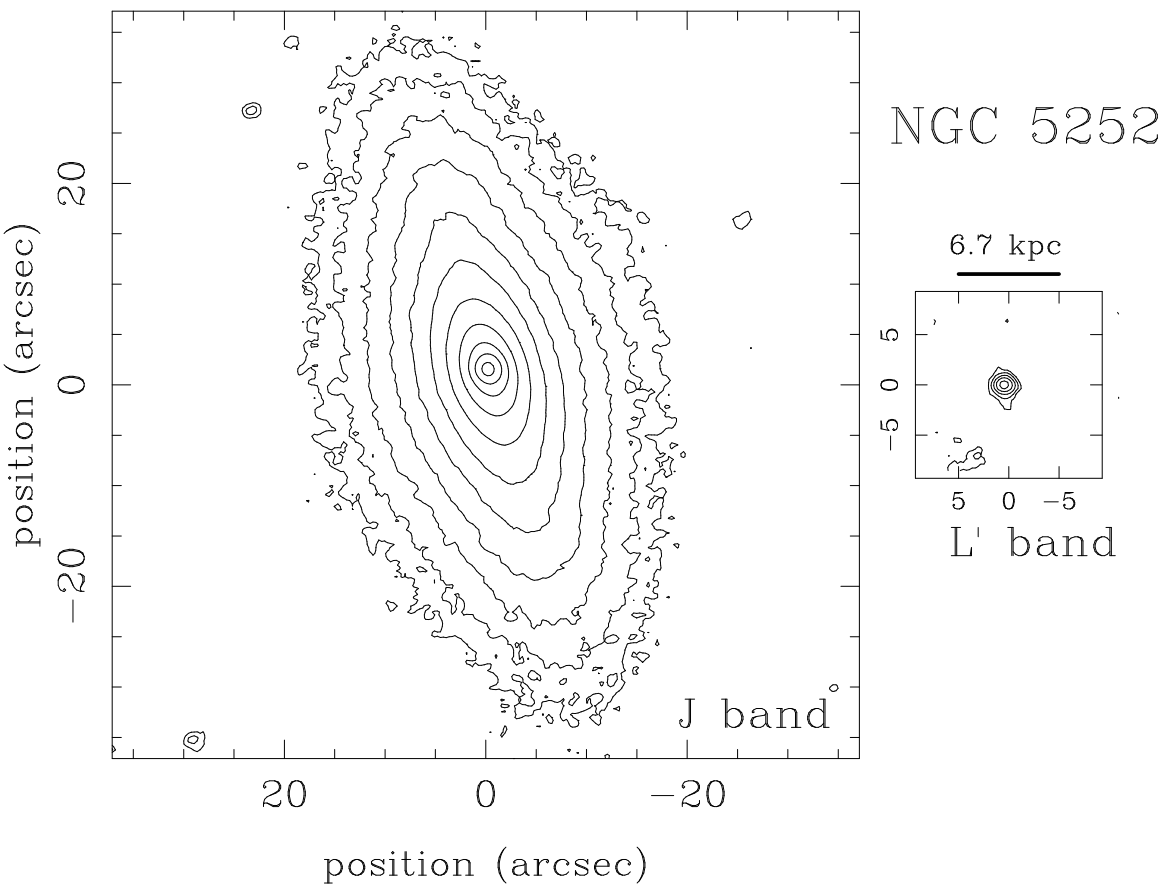
NGC 5252
6.7 kpc
J band
L' band
position (arcsec)
position (arcsec)
20
0
−20
5
0
−5

FIG. 1*k*

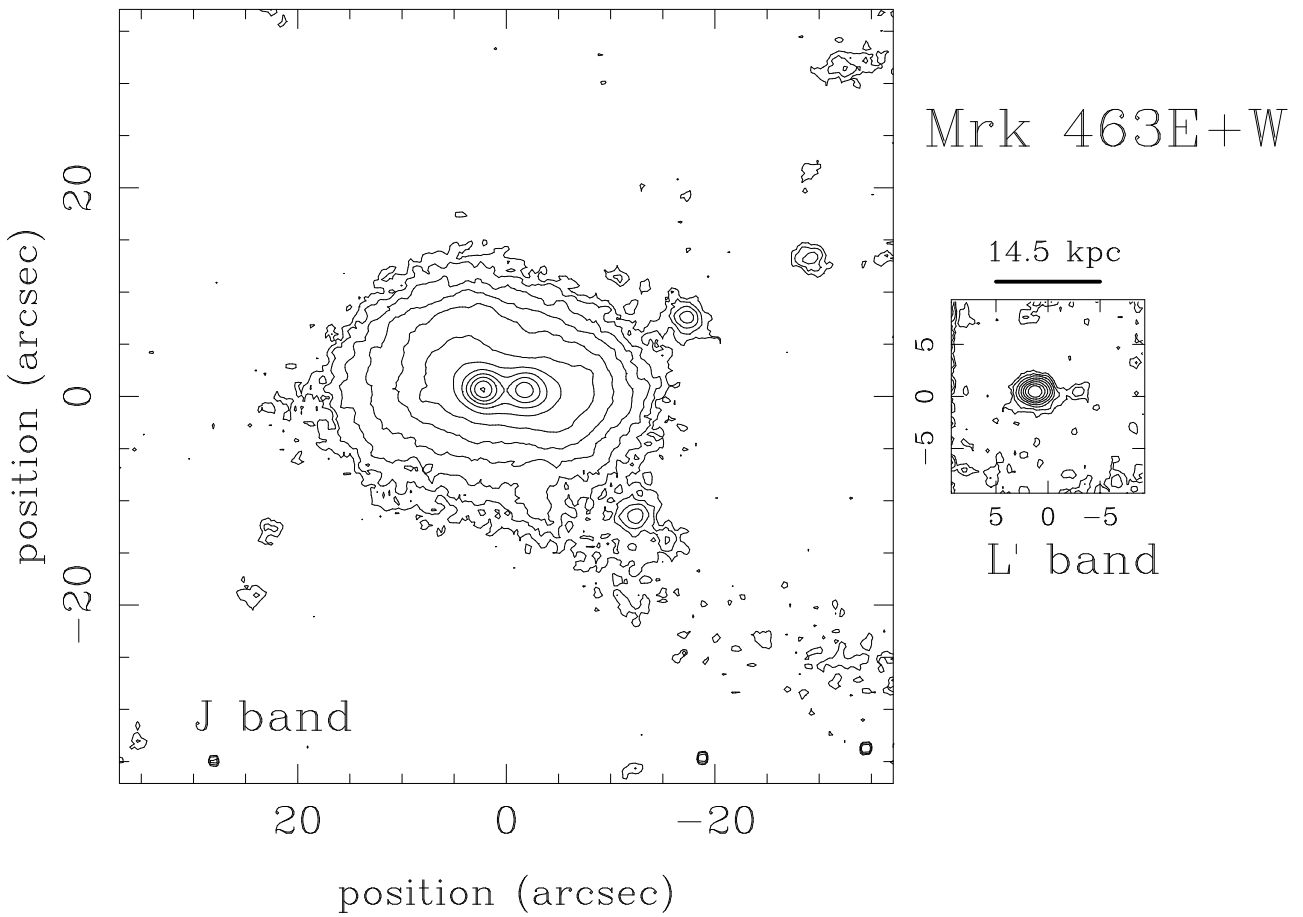

FIG. 1*l*

kpc. These two apertures are comparable to the size of the large-scale torus proposed by Maiolino & Rieke (1995). We have also computed the colors of the annuli with inner radii 0.5 kpc and outer radii 1 kpc. Table 3 lists the angular diameters (in arcseconds) and colors corresponding to the linear sizes 0.5 kpc and 1 kpc in the first and second rows, respectively, and the colors corresponding to the 0.5–1 kpc annulus in the third row. The listed errors include uncertainties due to both the photometric calibration and the determination of the sky level. Because of the large distance of Mrk 463E+W, we were not able to obtain its colors in 0.5 and 1 kpc diameter apertures; in the case of NGC 5252, we list only the 1 kpc and the 1–2 kpc annulus colors. For NGC 4388 we compute the 3″–6″ annular colors to match the size of the *L*′-band emission; for the assumed distance $d = 17.1$ Mpc, these colors correspond to an annulus 0.25–0.5 kpc.

Figures 2*a* and 2*b* show color-color diagrams, namely $J-H$ versus $H-K$ and $H-K$ versus $K-L$′. In each diagram, the circular/oval region to the left represents the colors of bulges of normal spiral galaxies, which match the colors of a late-type stellar population (Willner et al. 1984), whereas the circular/oval region to the right represents the typical colors of quasars corrected to zero redshift (Hyland & Allen 1982; Neugebauer et al. 1979). We have assumed a color transformation $L-L' = 0.15$ (Ward et al. 1982) when using photometry from previous work. The effects of 2 mag of visual extinction (Rieke & Lebofsky 1985) are represented by the arrow in the upper left-hand corner. The solid lines are the "mixing curves" that represent the colors of the sum of a late-type stellar population and either a blackbody component (presumed to be representative of hot dust) with temperatures $T = 600$, 800, 1000, and 1200 K (indicated next to the curves) or nebular emission (only in the $J-H$ versus $H-K$ diagram). The pure nebular component represents the colors produced by hydrogen and helium continuum and line emission (see Alonso-Herrero et al. 1996a for details). The numbers indicate the ratio of the dust luminosity to the stellar luminosity at *K*, $L_{\rm dust}/L_{\rm stell}$ (with loci shown by dashed lines) or the ratio of the nebular luminosity to the stellar luminosity. Open and filled circles represent the 0.5 and 1.0 kpc aperture colors, respectively, joined for each galaxy, while the starlike symbols are the colors of the annuli.

Figures 2*a* and 2*b* confirm the conclusion that the near-IR colors of the central regions of Seyfert 1.5–2 galaxies may be explained by a combination of emissions from an evolved stellar population and hot dust, possibly with some extinction effects. It is clear from both diagrams that the fraction of emission from the hot dust component increases for smaller apertures and must therefore be concentrated near the nucleus. The central $J-H$ and $H-K$ colors can be fully accounted for by emission from an evolved stellar population in only two galaxies—NGC 3081 and NGC 3393. For the rest of the galaxies, the $L_{\rm dust}/L_{\rm stell}$ ratios in the 0.5 kpc aperture are between $\simeq 0.5$ and $\simeq 3$.

TABLE 3

NEAR-IR COLORS FOR THE 0.5 AND 1 kpc DIAMETER APERTURES AND THE 0.5–1 kpc ANNULUS

Galaxy (1)	Aperture Diameter (arcsec) (2)	$J-H$ (3)	$H-K$ (4)	$K-L'$ (5)
Mrk 348	1.16	0.92 ± 0.10	0.77 ± 0.09	1.97 ± 0.09
	2.33	0.83 ± 0.10	0.61 ± 0.09	1.77 ± 0.09
	Ann	0.77 ± 0.10	0.48 ± 0.09	1.55 ± 0.11
Mrk 573	1.02	0.66 ± 0.10	0.67 ± 0.09	2.40 ± 0.09
	2.04	0.69 ± 0.10	0.55 ± 0.09	1.92 ± 0.09
	Ann	0.70 ± 0.10	0.49 ± 0.09	1.51 ± 0.09
NGC 1068.....	4.55	1.06 ± 0.10	0.92 ± 0.09	3.51 ± 0.09
	9.10	0.97 ± 0.10	0.74 ± 0.09	3.10 ± 0.09
	Ann	0.78 ± 0.10	0.42 ± 0.09	1.21 ± 0.10
NGC 2110.....	2.27	0.82 ± 0.10	0.87 ± 0.09	1.64 ± 0.09
	4.55	0.85 ± 0.10	0.62 ± 0.09	1.28 ± 0.09
	Ann	0.87 ± 0.10	0.43 ± 0.09	0.83 ± 0.11
NGC 2992.....	2.27	0.78 ± 0.10	0.82 ± 0.09	1.02 ± 0.10
	4.55	0.82 ± 0.10	0.55 ± 0.09	0.82 ± 0.13
	Ann	0.85 ± 0.10	0.46 ± 0.09	0.59 ± 0.15
NGC 3081.....	2.17	0.74 ± 0.10	0.34 ± 0.09	1.10 ± 0.11
	4.35	0.70 ± 0.10	0.29 ± 0.09	0.71 ± 0.13
	Ann	0.68 ± 0.10	0.26 ± 0.09	0.36 ± 0.20
NGC 3393.....	1.25	0.66 ± 0.10	0.31 ± 0.09	...
	2.50	0.66 ± 0.10	0.29 ± 0.09	...
	Ann	0.66 ± 0.10	0.28 ± 0.09	...
NGC 4151.....	4.17	0.94 ± 0.10	0.89 ± 0.09	1.84 ± 0.09
	8.33	0.88 ± 0.10	0.78 ± 0.09	1.80 ± 0.09
	ann	0.72 ± 0.10	0.35 ± 0.09	1.58 ± 0.14
NGC 4253.....	1.32	1.10 ± 0.10	1.10 ± 0.09	...
	2.64	1.04 ± 0.10	1.04 ± 0.09	...
	ann	0.99 ± 0.10	0.99 ± 0.09	...
NGC 4388[a].....	3.00	1.02 ± 0.10	0.68 ± 0.09	1.94 ± 0.10
	6.00	0.94 ± 0.10	0.52 ± 0.09	1.45 ± 0.15
	ann	0.88 ± 0.10	0.36 ± 0.09	0.33 ± 0.20
NGC 5252[b].....	1.50	0.72 ± 0.10	0.64 ± 0.09	2.02 ± 0.15
	ann	0.70 ± 0.10	0.47 ± 0.09	0.65 ± 0.20

[a] The apertures correspond to 0.25 and 0.50 kpc, and the 0.25–0.50 kpc annulus, respectively.

[b] Central colors corresponding to a 1 kpc aperture, circumnuclear colors within a 1–2 kpc annulus.

The most extreme colors are those of NGC 1068. The dust temperatures mostly range between $\sim$600 and 1200 K, which is in good agreement with the average $K-L'$ color temperatures (1040 ± 180 K) found by McAlary & Rieke (1988) for an X-ray–selected sample of Seyfert galaxies. When comparing these diagrams with Figures 4 and 5 in Alonso-Herrero et al. (1996b), where colors in a 3″ diameter aperture were plotted, it is noticeable that the scatter in the near-IR colors is significantly reduced. This reduction in scatter is likely the result of our plotting colors in apertures of a given *linear* diameter which are generally smaller than 3″. It is also clear from Table 2 that large aperture colors (i.e., those including most of the galaxy) tend to resemble the colors of normal spiral galaxies, except for NGC 4151 and NGC 4253, which still show quite red $H-K$ colors even in 30″ apertures. The $J-H$ and $H-K$ colors of the 0.5–1 kpc annuli are less affected by dust emission than those of the central regions and correspond quite well to the colors of normal galaxies; only the colors of NGC 4253 remain very red. In at least some galaxies (e.g., Mrk 348, Mrk 573, NGC 1068, and NGC 4151) the $K-L'$ colors of the annulus cannot be explained as emission from an evolved stellar population plus extinction effects. Rather, the annular $K-L'$ colors seem to reflect a combination of an evolved stellar population with hot dust in emission, with the fraction of K-band emission from hot dust being smaller than for the small nuclear aperture. The $K-L'$ colors of the annulus in NGC 2110, NGC 2992, NGC 3081, NGC 4388, and NGC 5252 could be simply the colors of an evolved stellar population reddened by a foreground extinction of $A_V \simeq 2$–4 mag.

Although the above model successfully explains the observed nuclear colors, a more realistic model in the context of the unified model would be desirable. Different geometries and physical sizes have been proposed for the hot dust close to the central engine, including a warped thin disk (Sanders et al. 1989) and a dusty torus extending over a few hundred parsecs in which the hot dust is located in the inner wall (Krolik & Begelman 1988; Pier & Krolik 1993; Granato & Danese 1994; Maiolino & Rieke 1995). In the dusty torus scenario the existence of differential reddening between the stars and the hot dust is predicted, since the torus maybe optically thick even in the mid-IR. Here we examine the possibility that the near-IR colors are produced by a combination of starlight not significantly reddened ($A_V \leq 2$ mag) and hot dust much more reddened ($A_V \simeq$ 0–40 mag). The results are illustrated in Figures 2*c* and 2*d*, which again are color-color diagrams. In each plot, the dashed line shows how the color changes as the ratio of the intrinsic (unobscured) dust luminosity at K to the stellar

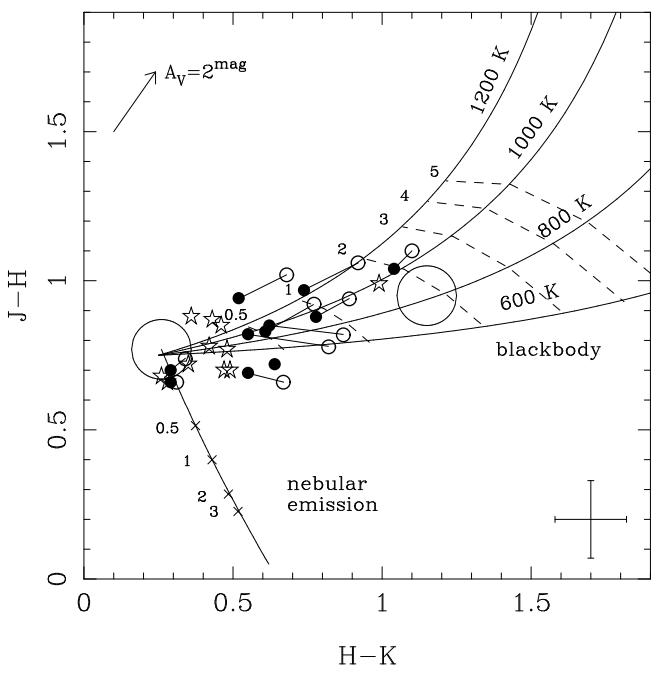

FIG. 2*a*

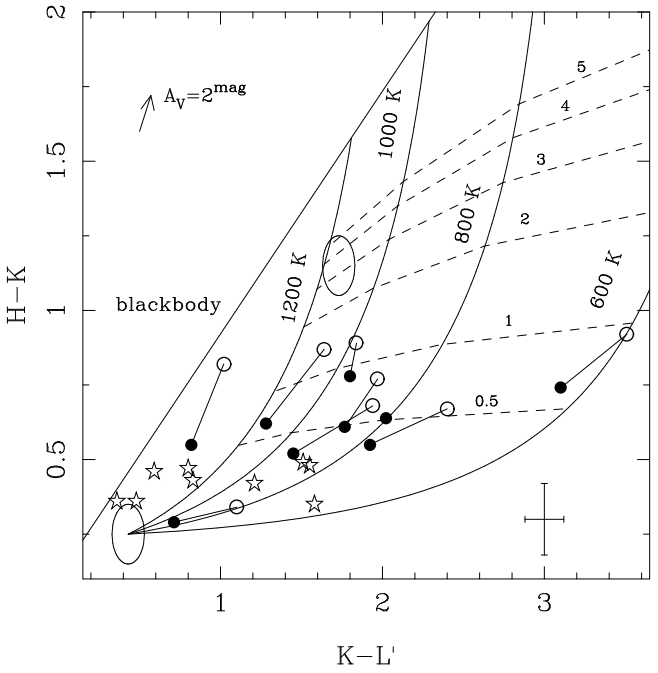

FIG. 2*b*

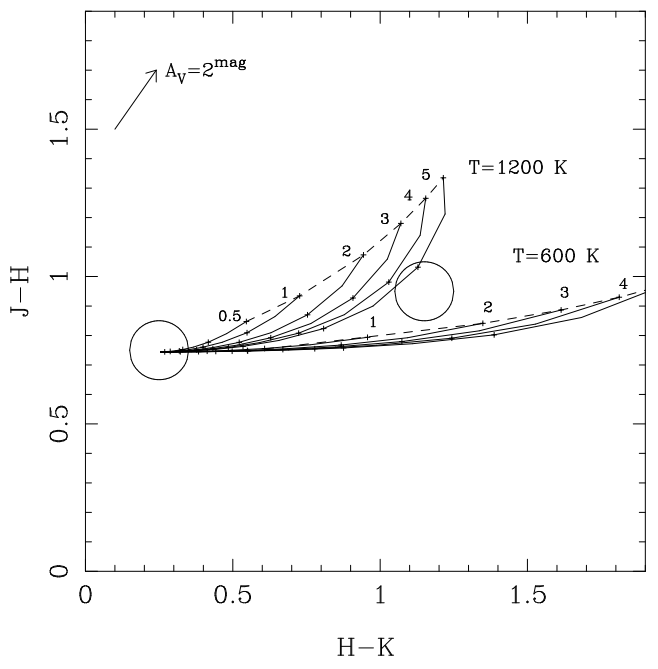

FIG. 2*c*

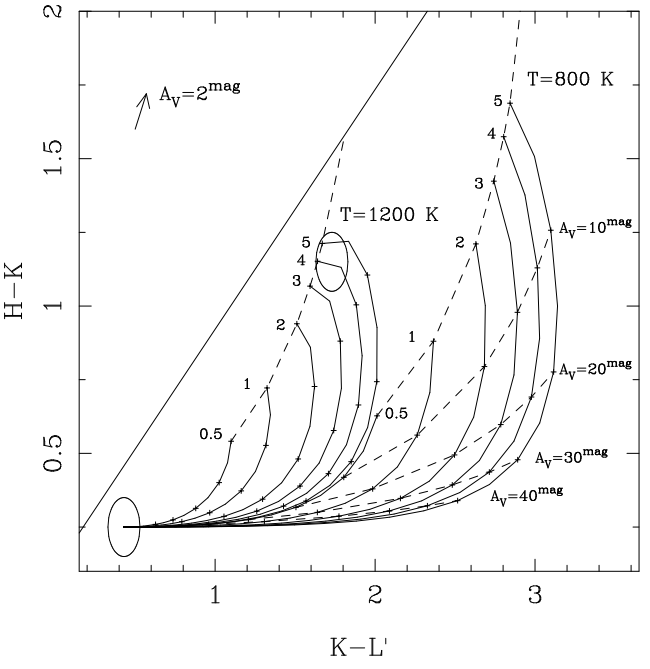

FIG. 2*d*

FIG. 2.—(*a* and *b*) $J-H$ vs. $H-K$ and $H-K$ vs. $K-L'$ diagrams. Open and filled circles are the 0.5 and 1 kpc aperture colors, respectively, while starlike symbols represent the circumnuclear (0.5–1 kpc annulus) colors. Maximum errors (which apply to the annular colors) are plotted in the lower right part-hand part of the diagrams: $\Delta(J-H) = 0.13$, $\Delta(H-K) = 0.12$, and $\Delta(K-L') = 0.12$ mag. See text for a detailed explanation of the mixing curves and other symbols. (*c* and *d*) $J-H$ vs. $H-K$ and $H-K$ vs. $K-L'$ diagrams showing the effects of differential extinction between the stars (unreddened) and the hot dust emission (reddened by $A_V = 0$–40 mag). The numbers next to the curves indicate the ratio of the dust emission to the galaxy emission (L_{dust}/L_{stell}). See text for details.

luminosity at K is varied: $L_{dust}/L_{stell} = 0.5$–5 (numbers next to the curves). These dashed lines correspond to the solid lines in Figures 2*a* and 2*b*. In Figures 2*c* and 2*d* we plot only the results for two dust temperatures: $T = 1200$ and 600 K in $J-H$ versus $H-K$ and $T = 1200$ and 800 K in $H-K$ versus $K-L$. The solid lines represent the mixing curves of the colors of a normal spiral galaxy (unobscured) and the colors of hot dust emission (reddened by visual extinctions from $A_V = 0$ to $A_V = 40$ mag) for the different ratios of dust emission to the galaxy emission in K. On these lines, the tick marks are located every 10 mag of visual extinction. Foreground reddening is indicated by the arrow on the

upper left-hand corner. Note that in Figure 2*d* the dashed lines for the 800 K mixing curve illustrate how the $L_{\rm dust}/L_{\rm stell}$ ratio changes for the various assumed dust extinctions. These results can be readily compared with the data plotted in Figures 2*a* and 2*b*. Clearly, most of the 0.5 kpc nuclear $J-H$, $H-K$, and $K-L'$ colors can be also explained as being produced by a mixture of an old stellar population and hot dust emission with a temperature $T = 1200$ K, the latter component reddened by between $A_V \approx 5$ and ≈ 30 mag. The ratio of dust emission to the stellar emission, as derived from these diagrams of the nuclear colors, is between $L_{\rm dust}/L_{\rm stell} = 1$ and 6 in Figure 2*c* and between $L_{\rm dust}/L_{\rm stell} = 0.5$ and 10 in Figure 2*d*. The 1 kpc colors are reproduced with the same dust temperature and A_V, but with smaller values of $L_{\rm dust}/L_{\rm stell}$. Only the nuclear colors of NGC 1068 require a lower dust temperature ($T = 800$ K), with $L_{\rm dust}/L_{\rm stell} \approx 10$ and $A_V \approx 25$ mag. The derived dust temperature for NGC 1068 agrees quite well with the effective dust temperature fitted by Pier & Krolik's (1993) models. Note, however, that although the models incorporating the extincted dust emission do not provide in general statistically better fits than the models with a mixture of stellar light and unreddened dust, they provide a better constraint to the dust temperature.

Since the emission from hot dust seems to make a significant contribution to the observed NIR colors of our sample of Seyfert galaxies, one expects that the NIR spectroscopic absorption features of stars should be diluted by the nonstellar continuum. The dust emission clearly dilutes the CO band (at 2.29 μm) in the nuclear spectrum of NGC 1068 (see Fig. 3 in Origlia, Moorwood, & Oliva 1993), with a nonstellar contribution at 2.29 μm of about 83% or equivalently $L_{\rm dust}/L_{\rm stell} = 4.9$. This result is in good agreement with our two limiting estimates for the ratio of dust emission to the stellar emission in K from Figures 2*b* and 2*d*, that is, $L_{\rm dust}/L_{\rm stell} = 1$, $T({\rm dust}) = 600$ K for the unreddened dust model, and $L_{\rm dust}/L_{\rm stell} = 10$, $T({\rm dust}) = 800$ K for the model with extincted dust ($A_V = 25$ mag). For NGC 2110, Oliva et al. (1995) estimate that the stars contribute approximately 80% of the total continuum at 2.29 μm or $L_{\rm dust}/L_{\rm stell} = 0.25$ for a slit of 4″. From our 1 kpc aperture photometry we infer $L_{\rm dust}/L_{\rm stell} = 0.50$ with no significant A_V for the dust, consistent with the finding of Oliva et al. (1995).

So far we have compared the NIR colors of our sample of Seyfert galaxies with the expectations for normal galaxies. However, it is of interest to compare the actual surface brightnesses on the scales probed (e.g., radius 0.5 kpc, and the 0.5–1 kpc annulus). Peletier & Barcells (1997) present NIR surface brightness profiles of a complete sample of 30 nearby S0–Sbc galaxies. We have compared the K-band surface brightness profiles of the Seyfert galaxies with those of spiral galaxies with similar morphological type and redshift. For all our Seyfert galaxies except NGC 1068, NGC 4151, and NGC 4253, we find surface brightness profiles similar to those of spiral galaxies, with differences ranging from 0.1 to 0.8 mag arcsec^{-2} for radial distances between 0.5 and 1 kpc, and for the inner 0.5 kpc. The surface brightnesses of the Seyfert galaxies NGC 1068, NGC 4151, and NGC 4253 at 0.5–1 kpc radius are 1–2 mag arcsec^{-2} brighter than the normal galaxies. Interestingly, these three galaxies show the reddest $H-K$ colors for the 0.5 and 1 kpc diameter apertures. From our small sample of Seyfert galaxies, we cannot, however, derive any statistically significant conclusions as to whether the surface brightnesses of the nuclear and circumnuclear regions of Seyfert galaxies are substantially brighter than those of normal galaxies.

3.2. *The L′-Band Imaging*

Thermal imaging ($\lambda > 3$ μm) has number of advantages over shorter near-IR wavelengths for studying the nonstellar light at the center of active galaxies. It has already been shown that contamination by stellar emission is much smaller at L' (or L) than at shorter wavelengths; the nonstellar contribution at L' is between 30% and 90% of the total emission in apertures with sizes between 3″ and 10″ (McAlary & Rieke 1988; Alonso-Herrero et al. 1996b). In addition, dust with an equilibrium temperature $T \simeq 1000$–1300 K has its emission peak close to 3 μm. A few L'-band (or L-band) imaging studies of active galaxies have shown that the nuclear sources appear to be very compact at this wavelength with only a very small contribution from the host galaxy. Examples of such compact sources include the radio galaxies Cygnus A (Djorgovski et al. 1991), Centaurus A (Turner et al. 1992), and PKS 0634−205 (Simpson, Ward, & Wilson 1995); the Seyfert 2 galaxies NGC 1386, MCG −5-23-16, and IRAS 19580−1818 (Alonso-Herrero et al. 1996b); and the Seyfert 1 galaxies NGC 7469 (Mazzarella et al. 1994) and Mrk 231 (Zhou, Wynn-Williams, & Sanders 1993).

When determining the nuclear contribution to the total emission from a galaxy at optical and near-IR wavelengths, the usual procedure involves deconvolving the profile into different components, typically an unresolved nuclear source, a bulge, and a disk. However, because of the compact nature of the sources and the small contribution from the underlying galaxy, such an approach is not feasible at L', and so a different method has been adopted. Our approach is similar to that used by McLeod & Rieke (1995) and Forbes et al. (1992) and involves the assumption that a point-spread function (PSF) from observations of a star is a good representation of the unresolved light from the nuclear point source. The azimuthally averaged radial surface brightness profile of the galaxy is first obtained. Owing to the small area covered by the L'-band images, there are no stars in the field, and therefore a standard star observed shortly before or after the galaxy is used for the PSF. The stellar PSF brightness profile is then scaled to match the central galaxy brightness. Note that in doing so we may overestimate the point-source brightness since there is some stellar flux at the nucleus itself. In Figure 3 we show four examples of the L'-band brightness profiles (expressed in mag arcsec^{-2}) represented as squares with their associated errors. The PSF brightness profiles are the starlike symbols. A Gaussian function has been fitted to each stellar PSF, with the value of the seeing in arcseconds (FWHM) indicated at the top of each panel. The Gaussian fit is represented by the dashed line.

The contribution of the unresolved source is found by integrating both the galaxy and standard star brightness profiles within two apertures: a fixed 3″ diameter aperture and an aperture comprising the surface brightness limit at L' as indicated for each galaxy in the caption of Figure 1. Finally the ratios of the unresolved to the total L' flux are calculated for both apertures. The results are presented in Table 4, where column (1) gives the name of the galaxy, column (2) gives the FWHM (in arcseconds) obtained by fitting a Gaussian function to the standard star, column (3)

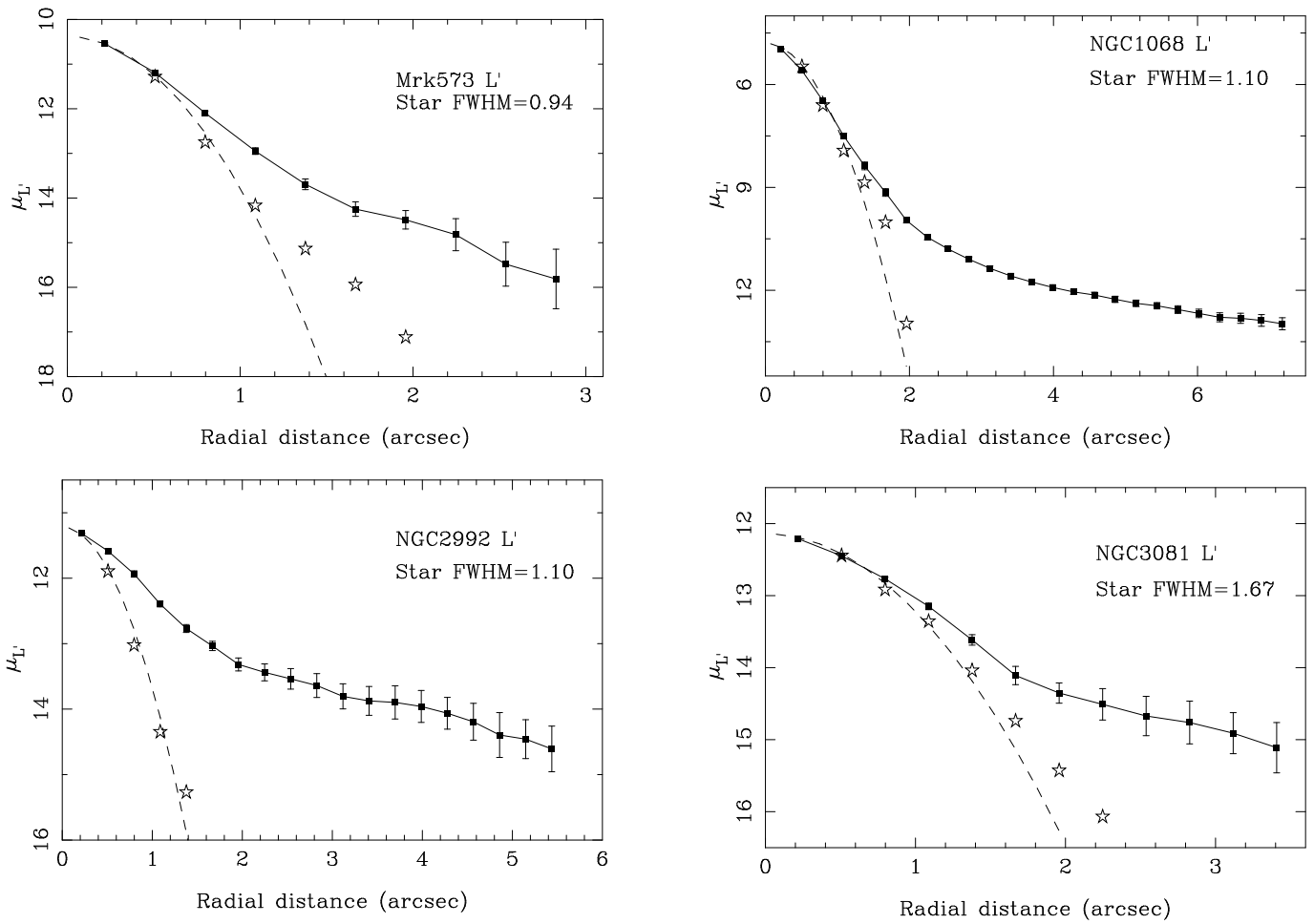

FIG. 3.—Surface brightness profiles (in mag arcsec^{-2}) in the L' band for four galaxies of the sample. The squares represent the observed galaxy data points with their associated errors. The starlike symbols are data points for the PSF brightness profile computed from the standard star observed shortly before or after the galaxy and scaled to match the central brightness of the galaxy. The data point spacing corresponds to the pixel size of the images, i.e., 0.″286 pixel^{-1}. The dashed line is a Gaussian function fit to the stellar profile.

gives the fraction of the total flux within a 3″ diameter aperture that is unresolved, column (4) gives the maximum radius used to produce the L' galaxy brightness profile, column (5) gives the fraction of the total flux within the aperture given in the previous column that is unresolved, and column (6) gives the magnitude of the unresolved source at L.

From Table 4 it can be seen that the contribution of the

TABLE 4

FRACTIONS OF THE PSF CONTRIBUTION IN THE L'-BAND WITHIN A 3″ DIAMETER APERTURE AND WITHIN THE L' SURFACE BRIGHTNESS LIMIT

Galaxy (1)	FWHM (arcsec) (2)	f_3 (%) (3)	r_{max} (arcsec) (4)	f_{tot} (%) (5)	$L'_{unr.}$ (mag) (6)	P.A.(J) (deg) (7)	P.A.(H) (deg) (8)	P.A.(K) (deg) (9)
Mrk 348[a]	0.94	91	2.6	74	10.7	99[c] ± 6	92[c] ± 6	97[c] ± 8
Mrk 573[a]	0.94	85	2.9	71	10.2	89 ± 1	87 ± 2	87 ± 1
NGC 1068[a]	1.10	100	7.5	85	4.5	46 ± 7	45 ± 7	42 ± 10
NGC 2110[b]	1.10	45	2.9	42	9.7	174 ± 3	173 ± 2	170 ± 3
NGC 2992[b]	1.10	43	6.5	26	11.0	38 ± 4	37 ± 4	39 ± 4
NGC 3081[b]	1.67	93	3.5	70	10.6	102 ± 5	103 ± 3	112 ± 4
NGC 3393[b]	...	...	...	...	...	160 ± 4	149 ± 4	142 ± 5
NGC 4151[a]	1.10	100	4.3	91	6.6	70[c] ± 7	75[c] ± 10	86[c] ± 7
NGC 4253[b]	...	...	...	...	...	102 ± 12	114 ± 8	104 ± 14
NGC 4388[b]	1.06	100	2.9	100	9.5	76 ± 1	77 ± 1	77 ± 3
NGC 5252[b]	0.94	91	2.6	77	11.1	18 ± 2	18 ± 2	15 ± 4
Mrk 463E[a]	0.94	85	2.0	83	8.2	...	...	...

NOTE.—Position angles of the major axes of the J-, H-, and K-band images are also given for a 5″ (1995 Jan data) and 3″ (1996 Dec data) diameter ellipse.

[a] P.A. from 1995 Jan data.

[b] P.A. from 1996 Dec data.

[c] P.A. values uncertain owing to the low value of the ellipticity.

unresolved source to the L'-band flux within a 3″ aperture exceeds 80% for all the galaxies in our sample except NGC 2992 and NGC 2110. In our sample, the unresolved source accounts for between 26% and 100% of the L'-band emission integrated over the brightness surface limit. This result was anticipated by the nonstellar fractions calculated by different methods, such as comparing the $K-L$ colors of normal galaxies and Seyfert galaxies (McAlary & Rieke 1988; Alonso-Herrero et al. 1996b). For the four galaxies in common with the study of Alonso-Herrero et al. (1996b)—NGC 2110, NGC 4388, Mrk 348, and Mrk 573—we find good agreement (to within the errors) for the contribution of the unresolved source to the integrated flux within a 3″ aperture.

3.3. *The Origin of the Circumnuclear L' Emission in NGC 1068 and NGC 4151*

As noted in § 3.1 there are four galaxies in our sample (NGC 1068, NGC 4151, Mrk 348, and Mrk 573) showing 0.5–1 kpc annular $H-K$ and $K-L'$ colors that cannot be accounted for with a reddened late-type stellar population. The angular size of the annulus used is small enough in the cases of Mrk 348 and Mrk 573 that the annular colors of these objects may be contaminated by the wings of the PSF. We therefore restrict our investigation of the nature of the circumnuclear L' emission to NGC 1068 and NGC 4151, which are both sufficiently close that we can rule out significant contamination to the annular colors from the nuclear source.

From Figure 2*b*, we estimate that about 80% of the K-band flux in the annuli of NGC 1068 and NGC 4151 is stellar in origin and that the remainder comes from dust with a temperature $T \approx 800$ K. We determine the excess (nonstellar) flux at L' by assuming a color $K-L' = 0.45$ for the stellar population. In this manner, we estimate that the L' luminosity of the extended nonstellar component is $\sim 10\%$ that of the nucleus at this wavelength. We investigate four mechanisms for the production of this circumnuclear emission.

First, we consider the possibility that the dust grains are heated by, and in thermal equilibrium with, the active nucleus. This is readily ruled out since equation (4) of Barvainis (1987) indicates that for 800 K dust to be in thermal equilibrium with the radiation field from the nucleus at a distance of 0.5 kpc requires a nuclear luminosity in excess of 10^{49} ergs s^{-1}, an order of magnitude greater than that of the most luminous quasars.

Simpson et al. (1996) found a similar problem when attempting to explain a red "bar" in Mrk 348. They proposed transient heating of small dust grains by reprocessed X-rays from the nucleus, and we examine the feasibility of that mechanism here. In their scenario, X-rays from the active nucleus are reprocessed into ultraviolet photons that heat the dust grains to several hundred kelvins. Their calculations for Mrk 348 show that the luminosity of this bar at 3.8 μm can only be a small fraction ($\lesssim 2\%$) of the intrinsic luminosity of the active nucleus at this wavelength. Although apparently at odds with the observed ratio of $\sim 10\%$, we note that many important numbers relating to grain destruction and accretion are not well known, and consequently we feel that it would be unwise to rule out this rather complicated scenario.

A third possibility is that the light is nuclear radiation scattered into our line of sight. Given the conclusion above that the L' luminosity of the extended nonstellar component is $\approx 10\%$ of that of the nucleus, scattering of light from the Seyfert nucleus is also implausible, since *all* of the light within a cone of opening angle 50° would have to be scattered into our line of sight.

Finally, we consider in situ heating of dust by hot stars. If the dust is concentrated close to the stars, the equilibrium temperature of the grains is potentially large enough for them to radiate substantial L' emission, unlike the situation when the Seyfert nucleus is the heating source (see above). In order to determine whether this is an energetically feasible process, it is necessary to determine the efficiency, η, with which dust can transform stellar radiation into thermal emission at 800 K. Within an optical depth $\Delta\tau$, a fraction,

$$f = \frac{\Omega}{4\pi}\left(1 - e^{-\Delta\tau}\right), \tag{1}$$

of the incident radiation will be absorbed by dust grains. For dust grains in thermal equilibrium with the radiation field,

$$\frac{L_{\rm rad}}{4\pi r^2}\, e^{-\tau} Q_a = 4 Q_e \sigma T^4, \tag{2}$$

where τ is the optical depth and Q_a and Q_e are the grain absorption and emission efficiencies, respectively. Assuming Q_a and Q_e are independent of r, the change in optical depth, $\Delta\tau$, from a temperature T_1 at radius r_1 to a temperature $T_2 < T_1$ at radius $r_2 > r_1$ is therefore

$$e^{-\Delta\tau} = \left(\frac{r_2}{r_1}\right)^2 \left(\frac{T_2}{T_1}\right)^4, \tag{3}$$

and so,

$$f \le \frac{\Omega}{4\pi}\left[1 - \left(\frac{T_2}{T_1}\right)^4\right], \tag{4}$$

where the equality occurs only for a geometrically thin sheet of dust.

The above discussion is true for *any* dust distribution. From Figure 2*b*, we determine $T \approx 800$ K as a typical temperature for the dust. For dust at this temperature, approximately 11% of the thermal emission (assuming the dust radiates as a blackbody) appears in the L' window (which covers the range 3.5–4.1 μm). This fraction is almost completely independent of temperature for $700 < T < 1500$ K, and so we have that

$$\eta = 0.11 f \le 0.11\, \frac{\Omega}{4\pi}\left[1 - \left(\frac{T_2}{T_1}\right)^4\right]. \tag{5}$$

The estimated dust luminosities within the 0.5–1 kpc annulus are $1.63 \pm 0.10 \times 10^{42}$ ergs s^{-1} and $6.09 \pm 0.10 \times 10^{41}$ ergs s^{-1} for NGC 1068 and NGC 4151, respectively. Putting $\Omega = 4\pi$, $T_1 = 1000$ K, and $T_2 = 800$ K (the calculation is fairly insensitive to the exact choice of temperatures, varying by no more than a factor of 2 for any reasonable temperature range), we derive lower limits to the required UV luminosities of 1.7×10^{43} ergs s^{-1} and 6.4×10^{42} ergs s^{-1}, respectively. Fanelli et al. (1997) have recently observed both galaxies with the Ultraviolet Imaging Telescope and showed that they display extended UV emission suggesting the presence of massive star formation in their host galaxies. They determine that the starburst

disk of NGC 1068 dominates the observed UV luminosity ($\simeq$80%), whereas the disk of NGC 4151 contributes about 20% of the total UV luminosity. The UV luminosities of the disk emission are $L_{UV}(\text{disk}) \simeq 3.4 \times 10^{43}$ ergs s^{-1} and $L_{UV}(\text{disk}) \simeq 7.0 \times 10^{42}$ ergs s^{-1}, respectively, which would suffice to account for the annular L' emission in these two galaxies. This emission, however, is spread over a large region of the disk, whereas we require the equivalent heating power of 10^4–10^5 O stars to lie within 1 kpc radius. Since almost the entire UV luminosity of these stars would be converted into thermal dust radiation, they would not appear in Fanelli et al.'s images, and, in fact, their presence would be hard to detect independently. We consider in situ heating of dust by a circumnuclear starburst to be the least implausible of the four mechanisms we have considered for producing the annular L' emission.

3.4. *Morphology of the Central and Circumnuclear Regions*

Mulchaey & Wilson (1995) have found a good correlation between the orientations of the [O III] λ5007 emission-line region and the green continuum on a scale of a few arcseconds in a sample of Seyfert galaxies and have suggested that this is due to the presence of an extended featureless continuum component. Such an extended featureless continuum was originally proposed by Tran (1995) in order to explain the optical polarizations seen in a sample of Seyfert 2 galaxies.

McLeod & Rieke (1995) have found that the rate of occurrence of bars in Seyfert galaxies is similar to that in normal galaxies. However, Maiolino et al. (1997) find that asymmetries (namely, the occurrence of bars, interactions, and distorted morphologies) are more frequently present in hosts of Seyfert 2 nuclei than in field galaxies and in some cases are probably linked to an enhanced rate of star formation. Moreover, recent optical and near-IR surface photometry studies of galaxies selected as candidates for having at least double bars (see, for instance, Wozniak et al. 1995; Friedli et al. 1996) have shown that the proportion of Seyfert galaxies among these double-barred systems is high. These conflicting results are undoubtedly due to the subjective nature of what constitutes a distortion. This naturally raises the question of whether such structures are more common in Seyfert galaxies than in otherwise similar normal galaxies. In addition, small-scale red structures have been detected in near-IR color maps of the central or circumnuclear regions of some Seyfert galaxies (e.g., NGC 5252—Kotilainen & Prieto 1995; Mrk 348—Simpson et al. 1996) or in residual images obtained after subtracting a smooth model based on fitting elliptical isophotes to near-IR images (e.g., NGC 7469—Mazzarella et al. 1994; NGC 985—Appleton & Marcum 1993) or in optical images obtained with *HST* (e.g., NGC 5252—Tsvetanov et al. 1996; Mrk 573—Capetti et al. 1996).

It is of interest, then, to study in detail the morphologies of the central and circumnuclear regions of our sample of galaxies in order to determine whether or not there is an alignment between the near-IR continua and the EELRs (including ionization cones) and whether bars and red structures such as those mentioned above are commonly present in Seyfert galaxies with EELRs. To determine the morphology of obscuration and/or the presence of large-scale stellar bars, we have built smooth models of the J- and K-band images. For those galaxies observed during both runs, the isophotal analysis has been performed on both sets of images. Models consisting of best-fitting elliptical isophotes were constructed (by using the IRAF ELLIPSE routine) in order to reproduce the radial brightness profile, ellipticity, and the orientation (P.A.) of the galaxy. The J- or K-band image of each galaxy was then divided by the model, which is assumed to represent the stellar brightness distribution. The resulting images will reveal any isophotal deviations from elliptical symmetry, such as bars, spiral arms, H II regions, etc. This surface photometry technique used in the near-IR has proved to be extremely useful for both tracing the old stellar population and detecting bars and disks (Friedli et al. 1996). In Table 4, columns (7), (8), and (9), we give the P.A. of the 3″ diameter (major axis) isophote in the J, H, and K bands for those galaxies observed with the smaller pixel size (1996 December data) and for a 5″ diameter isophote for the 1995 January data. We chose a larger diameter for the latter data because, as mentioned in § 2, wind shake produced artificial elongations in some images, so that the shapes of the innermost isophotes may not be reliable. In Figure 4 we show plots of the surface brightness profile, ellipticity, and P.A. as a function of the semimajor axis of the fitted ellipse in J for each galaxy in our sample except Mrk 463E+W. When data existed from both observing runs, we plot both fits. In all cases we find an excellent agreement for the fitted ellipticity and P.A. in the overlapping regions of the galaxy.

In what follows, the results obtained for each galaxy in our sample are examined for the presence of isophotal deviations from elliptical symmetry. The structures seen in the model-divided images are compared with those in optical line-emission images; the possible co-alignment of these structures with the axes of the EELRs, radio emission, and overall galaxy orientation is also examined. Although bars and other nonaxisymmetric structures are clearly revealed in the model-divided images, we also examine the P.A. and ellipticity plots to check that any such structures are not artifacts. According to McLeod & Rieke (1995), the existence of a bar is indicated when the ellipticity grows steeply with radius and then falls off to the ellipticity of the disk of the galaxy, and at the same time the P.A. remains constant over the range of increasing ellipticity. In Table 5 we give the orientation of the outer parts of the galaxy as derived from the ellipse fitting of the lowest isophotes (1995 December data) in column (2); the orientation of the outer parts of the galaxy derived from optical data in column (3); the P.A. of the [O III] λ5007 and radio emissions in columns (4) and (5), respectively; and references for the optical and radio data in column (6). Column (7) summarizes those structures found in the model-divided images and their corresponding orientations. We do not discuss NGC 4151 here because the continuum images are contaminated by diffraction spikes from the bright nucleus and are therefore not suitable for this kind of analysis.

3.5. *Notes on Individual Galaxies*

3.5.1. *Mrk 348*

The near-IR and optical properties of the Seyfert 2 galaxy Mrk 348 have been extensively discussed by Simpson et al. (1996). To summarize, after subtracting a model for the surface brightness of the galactic bulge, they found a red linear structure (interpreted as an edge-on disk) in the near-IR continuum which runs approximately 2″ (800 pc) east-west and is unresolved in the north-south direction. An *HST* [O III] λ5007 image (Capetti et al. 1996) shows that

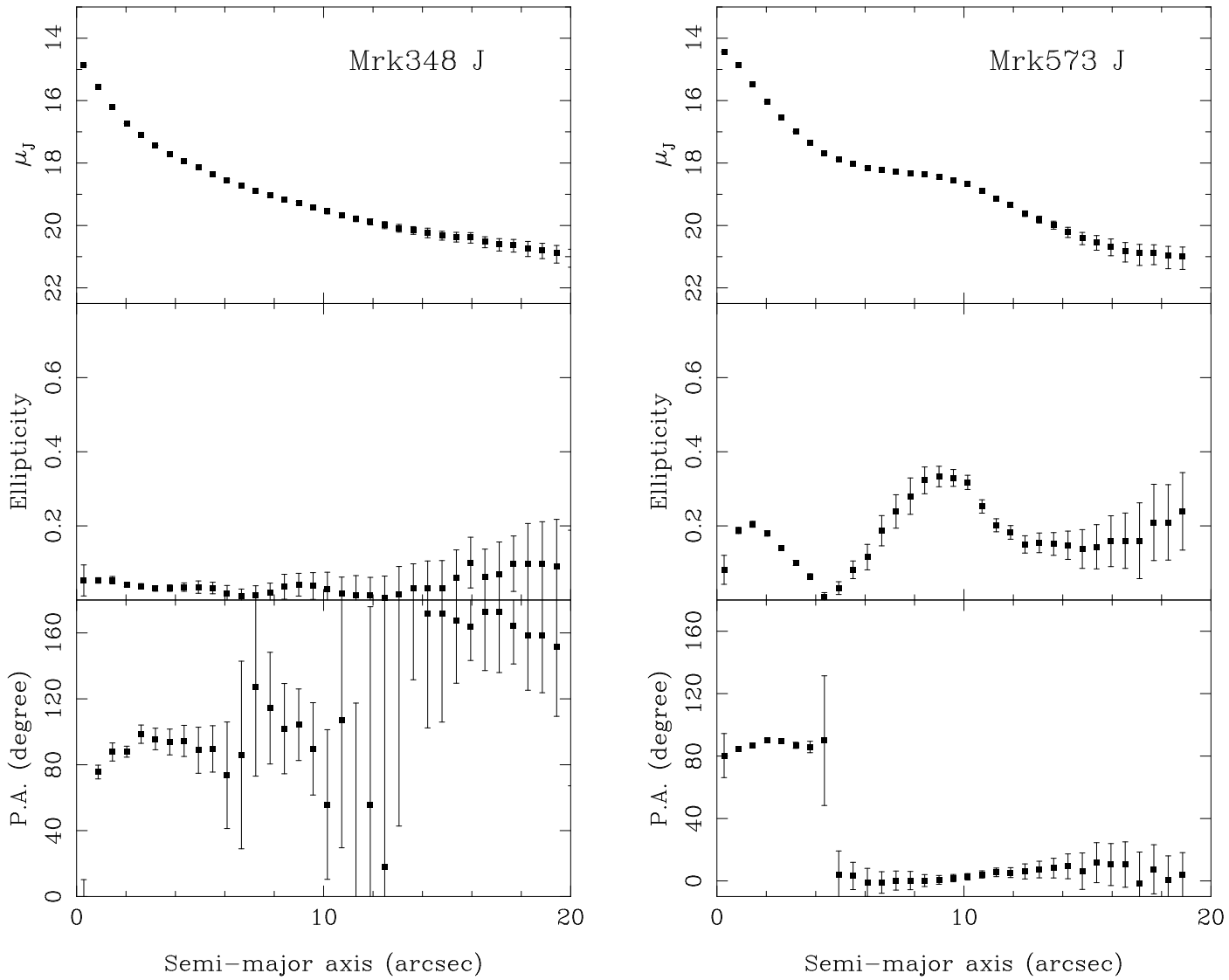

FIG. 4.—Surface brightness profile (in mag arcsec^{-2}), ellipticity, and major axis P.A. (and their corresponding errors) as a function of the semimajor axis of the fitted ellipse in the J band for each galaxy in our sample except Mrk 463. When the galaxy was observed during both runs, for the ellipticity and P.A. we plot the 1995 January data as filled squares and the 1996 December data as open circles.

the central emission is confined to a linear structure 0.″45 in size, with P.A. = 155°, while on a larger scale, the [O III] λ5007/Hα + [N II] emission is extended over several arcseconds and shows a biconical morphology with axis at P.A. $\approx$ 170° (Simpson et al. 1996; Mulchaey, Wilson, & Tsvetanov 1996). Capetti et al.'s (1996) optical continuum image reveals obscuration across the nuclear region with a scale of less than 50 pc. The resolution of our images is not good enough to determine whether this obscuration is associated with the elongated red feature seen in the near-IR images.

In Figure 4*a* we show the ellipticity and major axis P.A. as a function of the semimajor axis of the fitted ellipse in the J band. The P.A. of the 5″ scale isophote in the J-, H-, and K-band images is close to 90° (consistent with the orientation of the elongated red feature found by Simpson et al. 1996). However, the fitted P.A. should be taken with caution because of the low values of the ellipticity. Within a region of size equal to or smaller than 3″ (1.3 kpc), 90% of the L-band emission appears to be unresolved.

3.5.2. *Mrk 573*

When fitting elliptical isophotes to the J- and K-band images, a remarkable twist in the major axis of the isophotes is found at a radial distance of 4.″5 (see Fig. 4*b*), changing rapidly from P.A. $\simeq$ 0°–10° in the outer isophotes to P.A. $\simeq$ 80°–90° in the inner isophotes. This is consistent with the presence of a stellar bar extending over approximately 20″ (9.8 kpc) at P.A. = 0° as also found in the *HST* 5500 Å continuum image (Capetti et al. 1996). In addition to this large-scale bar, Pogge & DeRobertis (1995) find evidence for the presence of an inner stellar bar in this galaxy, oriented nearly east-west (P.A. $\simeq$ 100°), perpendicular to the large-scale bar. Our data support this result, since the ellipticity increases steeply from the nucleus out to radial distance $r \simeq 2''$, while the P.A. remains approximately constant (Fig. 4*b*). This galaxy therefore shows evidence for a "bar within bar" situation.

Capetti et al. (1996) constructed an axisymmetric model from the *HST* 5500 Å continuum image and found a dust lane that spans 1″ (500 pc) and is significantly warped. The

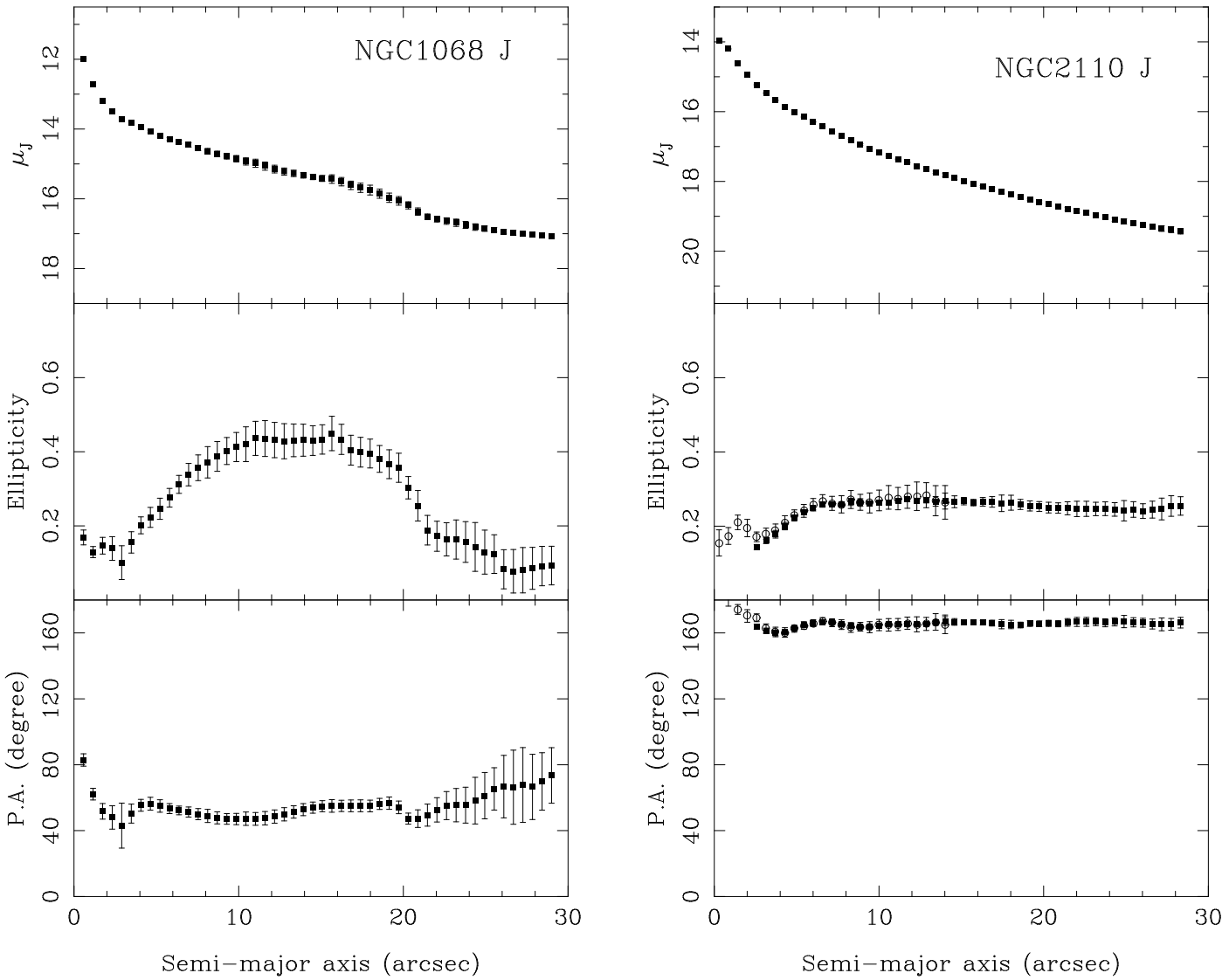

FIG. 4—*Continued*

variation of the P.A. and ellipticity with radius found by these authors compares well with our results; differences in the ellipticity of approximately 0.1 are found in the inner 2″. The *HST* [O III] λ5007 image (Schmitt & Kinney 1996) reveals emission extending 2″ to the northwest with a total opening angle of 70°, whose substructure is apparently dominated by the interaction of the radio jet with the ISM. The P.A. of the 5″ diameter ellipse at *J*, *H*, and *K* (Table 4) are all similar and consistent with the orientation of the inner bar.

3.5.3. *NGC 1068*

In Figure 5 (Plate 3) we present the *J*-band image divided by the model of NGC 1068 superimposed on the *J*-band continuum image (note that due to the brightness of this galaxy, the *K*-band image shows a ghost image of the nucleus, and therefore the fitting is not reliable at that position). The solid contours (emission in excess over the galaxy model) clearly show an impressive stellar bar and the inner spiral arms. The bar runs from northeast to southwest at position angle P.A. = 45°–50°, approximately 36″ (4 kpc) in extent, and between 3″ and 6″ (300–600 pc) in width, in good agreement with the results found by Thronson et al. (1989) at 1.6 and 2.2 μm. Furthermore, the resemblance of the deviations from the symmetric model to the "lumpy" morphology seen in the CO map presented by Helfer & Blitz (1995) is remarkable, although the P.A. of the molecular bar is slightly different ($\simeq 63°$). The orientation of the bar differs from the kinematic and photometric major axis of the galaxy disk (P.A. = 80° ± 9°; Baldwin, Wilson, & Whittle 1987). The [O III] λ5007 emission-line region of this galaxy has a conical shape extended by 7.″5 at P.A. = 35°, with opening angle 45° (Evans et al. 1991). The *L*′-band image shows emission within 5″ of the nucleus, with 85% of the total emission unresolved and associated with the nucleus, whereas the extended emission at this wavelength follows the orientation of the *J*, *H*, and *K* inner isophotes (Fig. 1*c*).

In addition to the bar, there is a ringlike structure or perhaps inner spiral arms in the *J*-band image, with outer diameter $\simeq 36''$, similar to the 10 μm structure found by Telesco et al. (1984) and the morphology in the UV/red continuum color map presented in Pogge & DeRobertis (1993). These authors show that roughly half of the mid-/

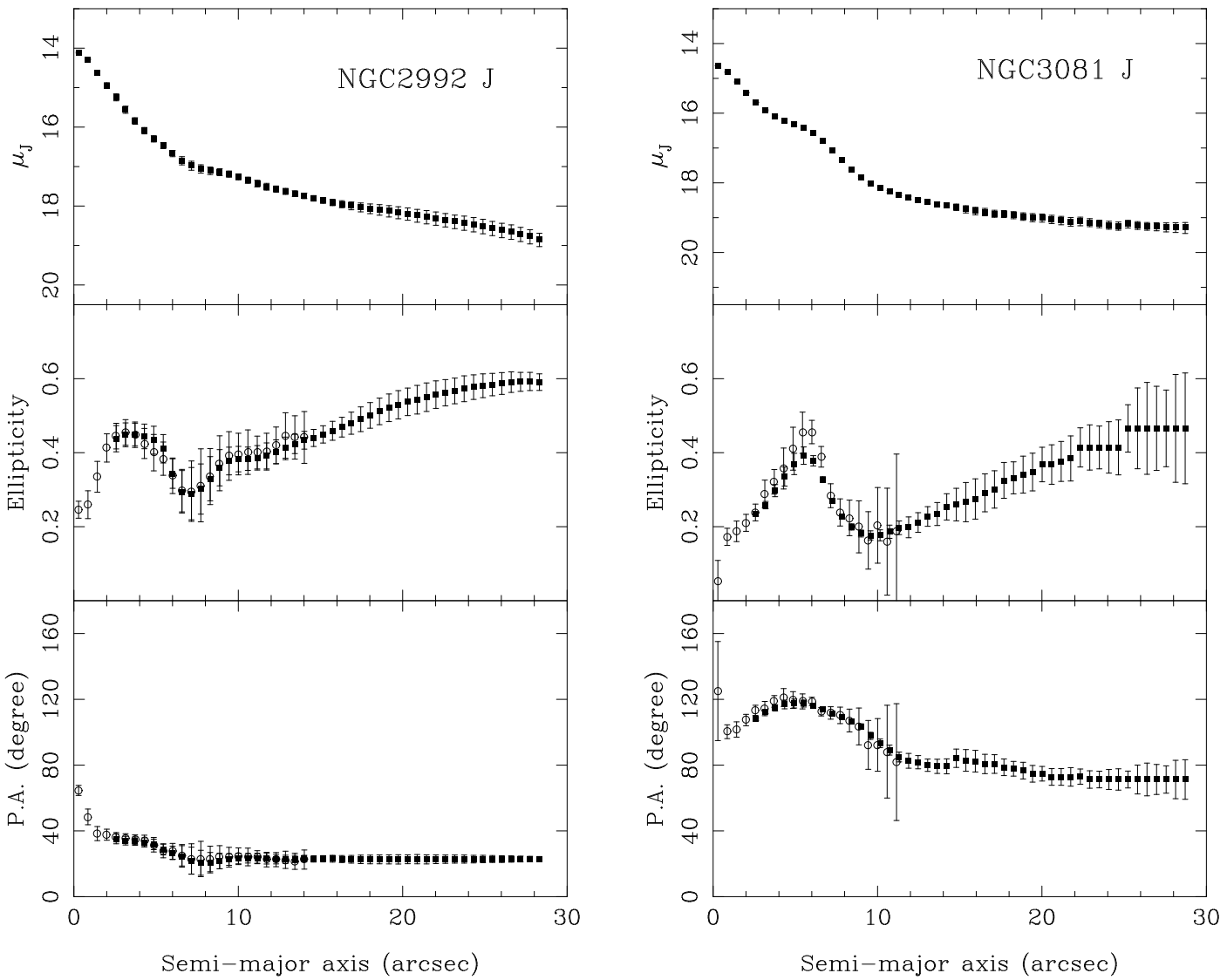

FIG. 4—*Continued*

far-IR emission from NGC 1068 originates from the Seyfert nucleus and half from the disk surrounding it, with the disk being powered by star formation. The near-IR colors within an annulus with inner diameter 30″ and outer diameter 36″ (i.e., bracketing the ring) are $J-H=0.78$ and $H-K=0.27$, consistent with the colors of normal spiral galaxies, whereas the colors of the nucleus itself (for a 3″ diameter aperture) are extremely red: $J-H=1.15$, $H-K=1.10$, and $K-L'=3.70$, and can best be represented in terms of a combination of unreddened starlight plus obscured hot dust emission (with a blackbody temperature $T\simeq 800$ K), as explained above. The ratios of the total fluxes in the ring to the nuclear emission (defined as the region interior to the stellar bar, within a 6″ diameter aperture) in the observed images are 0.80, 0.65, and 0.37 at *J*, *H*, and *K* band, respectively, which demonstrates the increasing dominance of the nuclear emission toward longer wavelengths.

3.5.4. *NGC 2110*

The central part of the *J*- and *K*-band model-divided images (not shown here) displays only an unresolved structure located at the center of the galaxy, and a red "blob" at a distance 9″ (2 kpc) from the center in the southeast direction, which is possibly an H II region or a foreground star. The major axis P.A. of the 3″ diameter isophote in the *J*, *H*, and *K* images is 170°–174°, with the major axis converging to 163° at larger radial distances, which coincides with the optical overall galaxy orientation of 160°–166° (Wilson et al. 1985). The contribution of the unresolved nucleus at *L'* appears to be smaller than for most galaxies in our sample, with the nucleus contributing only 42% of the total flux within a 3″ diameter aperture. The *HST* [O III] λ5007 emission-line image of this galaxy displays a curved extended emission morphology, which extends from the nucleus over 0.″7 along the northwest direction and then bends toward the northeast, with a total extent of 0.″9 (Mulchaey et al. 1994). The P.A. of the near-nuclear [O III] λ5007 and green continuum isophotes in ground-based images is 158° (Mulchaey & Wilson 1995) in good agreement with the near-IR P.A. at radial distances greater than 2.″7.

3.5.5. *NGC 2992*

NGC 2992 is an Sa galaxy seen almost edge-on and interacting with NGC 2993. The *K*-band image divided by the

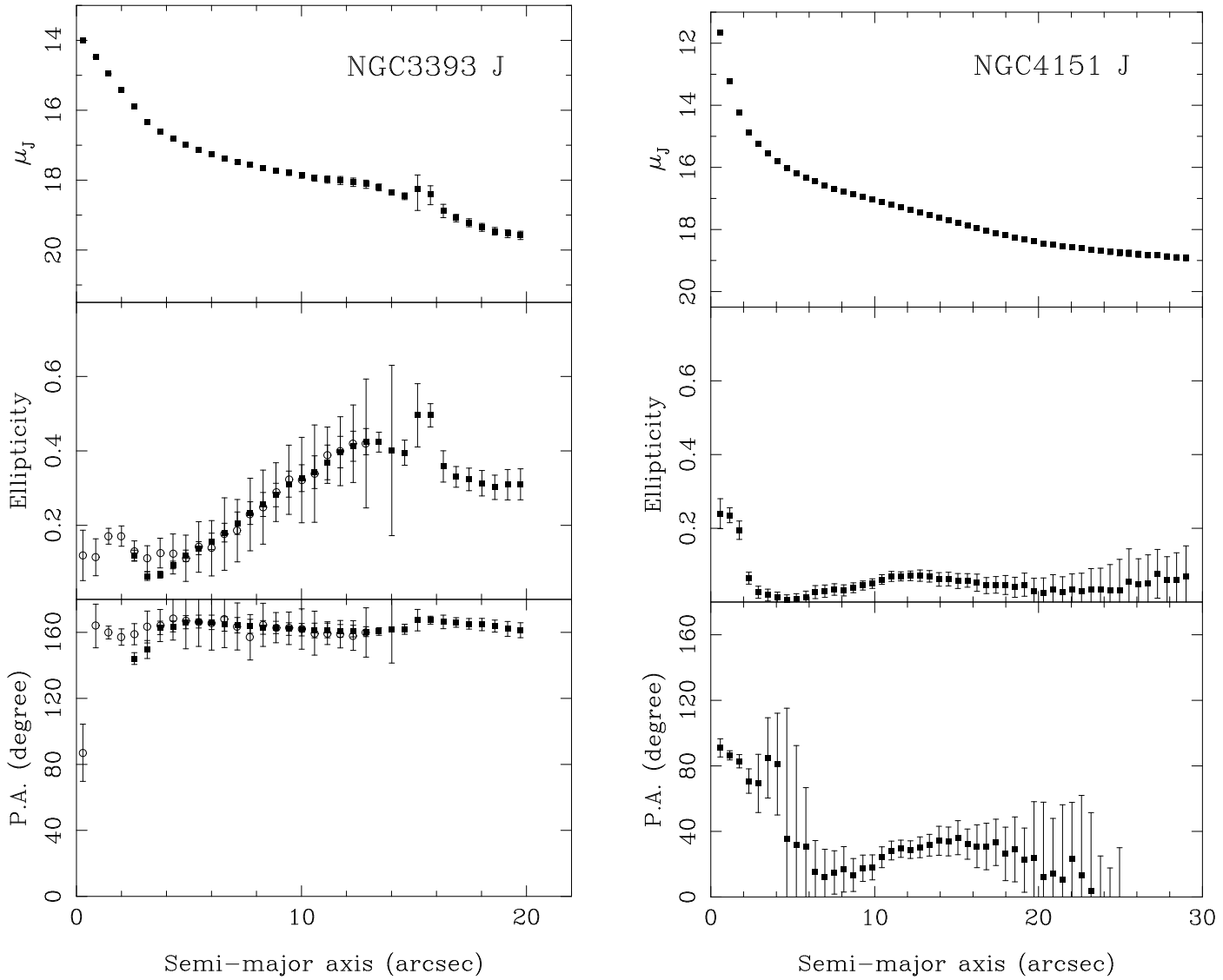

FIG. 4—*Continued*

model of NGC 2992 is presented in Figure 6 (Plate 4) (the image derived from the *J*-band data shows a similar morphology). The model-divided result for this galaxy displays a very complex structure. In the innermost regions, there is a structure at P.A. = 37° seen in excess, extending approximately 6″ (1.3 kpc) from the nucleus to the northeast and 11″ (2.4 kpc) to the southwest. The spiral arms are also visible. The overall galaxy orientation as derived from the P.A. plot is P.A. = 23° (see Fig. 4*e*).

The Hα + [N II] image presented in Colbert et al. (1996) shows the presence of a dust lane that separates the line emission into a double-lobed shape, extending about 5″–15″ in the southeast-northwest direction. A careful alignment of our model-divided image with the image in Colbert et al. (1996) shows that the location of the structure seen in our image does not correspond with the position of the dust lane. Owing to the high inclination of this galaxy, we cannot discern the nature of this structure. This galaxy also shows extended emission at *L* (Fig. 1*e*), with the contribution of the unresolved component to the total observed flux being relatively small (26%) in comparison with what is found for most of the galaxies in our sample. The P.A. of the 3″ isophotes in the *J*, *H*, and *K* bands are all consistent with the orientation of the dust lane, while at larger radial distances the P.A. become $\simeq$23°–26°, presumably tracing the underlying stellar distribution. The nuclear $K-L'$ colors of this galaxy are the least red of any in our sample because the L' unresolved component contributes a relatively small fraction of the total emission.

3.5.6. *NGC 3081*

The optical morphology of this galaxy is extensively discussed by Buta (1990), who found it to possess three rings of diameters 13″ (nuclear), 67″ (inner), and 150″ (outer) together with a weak bar which is enveloped by the inner ring. Our elliptical isophote analysis (performed out to a radial distance of 30″) appears to show two bars. Figure 7 (Plate 5) displays the *J*-band data results and shows the inner ring described in Buta (1990) in the continuum image (gray-scale). The nuclear bar has a P.A. = 117° (consistent with the P.A. of the nuclear bar in Buta's description), extending up to 6.″6 (1.5 kpc) on either side of the nucleus. The inner bar has an average P.A = 71°. The major axis position angle of this galaxy (i.e., orientation of the outer

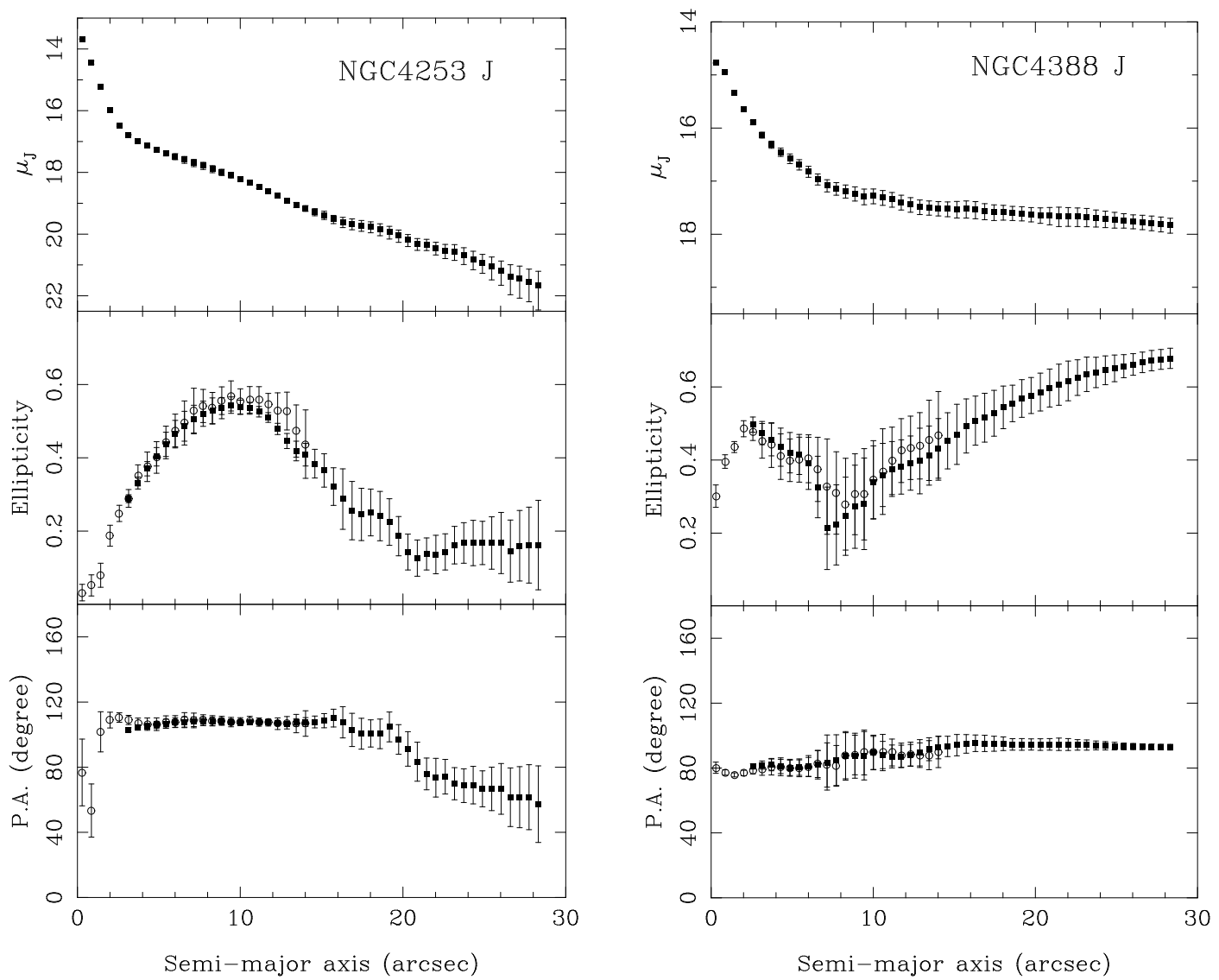

FIG. 4—*Continued*

ring) is P.A. = 123° ± 4° (Buta 1990). From the *J*-band continuum image, there is evidence for a ring of H II regions with inner diameter 45″ (10.4 kpc), whose orientation is consistent again with that of the inner bar. The bars and the rings show evidence for star formation according to Wozniak et al. (1995), who found similar structures in their optical continuum images; the isophotal analysis performed by Friedli et al. (1996) on near-IR images of this galaxy agrees quite well with our results. The Hα ground-based images obtained by Pogge (1989) and Storchi-Bergmann et al. (1996) show the H II regions of the inner ring congregating at the end of the inner bar. The Hα image of the nucleus appears to be rather asymmetric and extended along the major axis of the galaxy P.A. = 125° (Pogge 1989), with a diameter of 10″, and whose orientation and size are consistent with those of the nuclear bar seen in our images.

The P.A. values for the 3″ isophote in the *J*, *H*, and *K* bands are similar (102°–112°) but coincide with the P.A. of neither bar. The small-aperture $J-H$ and $H-K$ colors (see Tables 2 and 3) of this galaxy seem to be similar to those of elliptical or spiral galaxies with no signs of activity (see the study of the near-IR colors for galaxies of different morphological types in the Coma Cluster by Gavazzi & Trinchieri 1989), whereas the $K-L'$ color, although redder than that of a normal spiral galaxy, is much less red than the colors shown by other Seyfert 2 galaxies in our sample. The $J-H$, $H-K$, and $K-L'$ annular colors resemble those of a spiral galaxy. It is also noticeable that the near-IR colors do not show large changes with increasing aperture size.

3.5.7 *NGC 3393*

NGC 3393 is a SBab galaxy, the spiral arms of which form an almost complete ring. The *J*-band image presented in Figure 1*g* does not cover the full extent of the galaxy (the two bright objects located northwest of the center of the galaxy are stars according to Tsvetanov & Petrosian 1995). The faint outer spiral arms can be seen in the *J*-band image. The *J*-band model-divided image (Fig. 8 [Pl. 6]) traces the stellar bar along P.A. ≃ 160°–165°. A number of H II regions are seen at the end of the bar, with positions in good agreement with those found in Tsvetanov & Petrosian's image. The innermost regions of the model-divided image

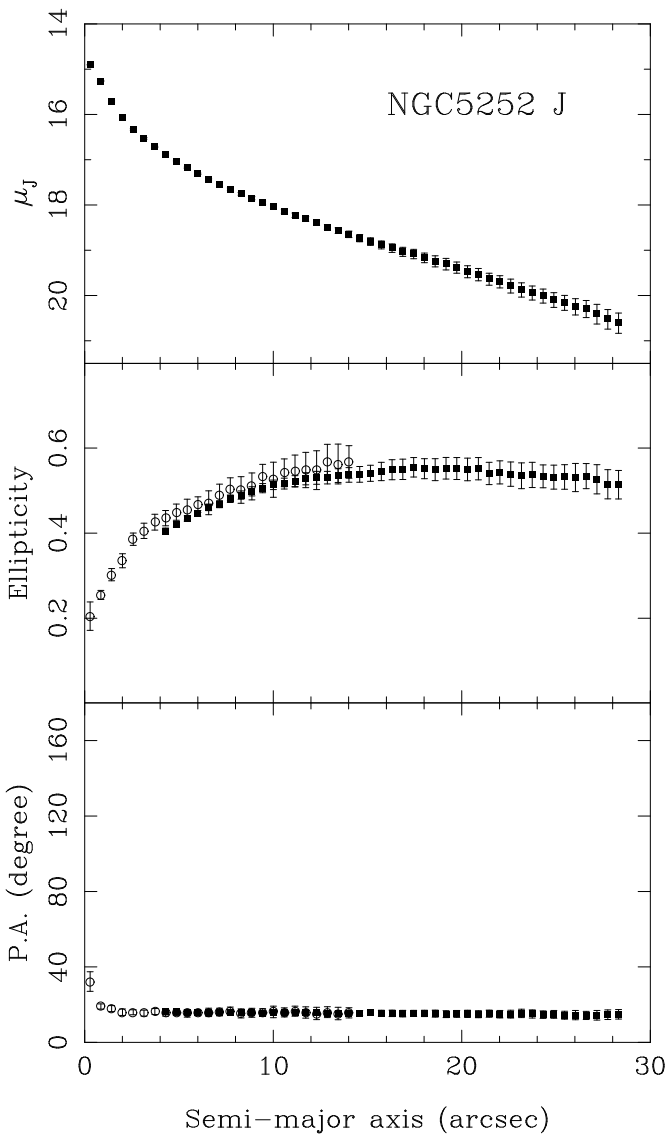

FIG. 4—*Continued*

display an unresolved central structure together with a linear structure (perhaps a faint bar) in P.A. $\simeq$ 145°–150°. The presence of the outer bar can be inferred from the variation of the ellipticity and P.A. as a function of the distance from the nucleus (Fig. 4*g*). The high-resolution *HST* [O III] λ5007 emission line image of this galaxy (Schmitt & Kinney 1996) reveals S-shaped emission extending 5″ along P.A. = 55°. The emission extends over 1.″8 on either side of the nucleus, roughly east-west, and then curves toward the north and south, in the same sense as the spiral arms.

The *J*-, *H*-, and *K*-band 3″ isophote P.A. values are 160°, 149° and 142° respectively, roughly perpendicular to the orientation of the [O III] λ5007 emission. NGC 3393 shows near-IR colors that resemble those of normal spiral galaxies or unreddened starbursts, with no evidence for dust emission or a large amount of extinction, even for the smallest aperture. We did not observe this galaxy at *L*′, but Boisson & Durret (1986) did and found that the near-IR emission is dominated by stellar emission, with no excess emission over their *L*-band stellar template.

3.5.8. *NGC 4253*

NGC 4253 (Mrk 766) is a barred SBa galaxy with optical overall orientation P.A. = 69° (MacKenty 1990). Indeed, the *J*-band model-divided image (see Fig. 9 [Pl. 7]; also seen in the direct image, Fig. 1*i*) clearly indicates the presence of a bar (i.e., positive galaxy minus model residuals) at P.A. $\simeq$ 110°, which may be compared with the P.A. $\simeq$ 60° of the outer isophotes. The bar reaches 7″ (2.7 kpc) to the southeast and 9″ (3.4 kpc) to the northwest, in good agreement with the size derived by McLeod & Rieke (1995). This galaxy also appears to have an asymmetric arm on its northern side that is well traced by the model-divided image, and a ringlike structure extending to the northeast, southeast, and west. The [O III] λ5007 morphology (Mulchaey et al. 1996) shows a core elongated east-west with fainter extensions in the northwest-southeast direction. The Hα line emission exhibits a plumelike structure to the east with line ratios well described by H II region models

TABLE 5

NEAR-IR, OPTICAL, AND RADIO POSITION ANGLES

Galaxy (1)	IR P.A. (deg) (2)	Optical P.A. (deg) (3)	[O III] P.A. (deg) (4)	Radio P.A. (deg) (5)	References for Optical and Radio Data (6)	Structure (7)
Mrk 348	...	111	170	170	1, 12, 13	R: 90°
Mrk 573	0–10	170–190	120	118	2, 2, 14	B: 85°, B: 0°
NGC 1068.....	47–55	80	35	33	3, 4, 14	B: 47°
NGC 2110.....	166	160–166	157	1	5, 6, 15	R (unresolved)
NGC 2992.....	23	...	−67*	−20	..., 7, 15	E: 35°
NGC 3081.....	71	123	125*	...	8, 1, ...	B: 117°, B: 71°
NGC 3393.....	161–167	...	55	55	..., 4, 16	B: 145°?, B: 160°
NGC 4151.....	...	22	55	92	9, 4, 15	R (unresolved)
NGC 4253.....	60	69	102	16	10, 6, 17	B: 108°
NGC 4388.....	95	90	35	26	11, 11, 14	...
NGC 5252.....	15	15	1	−15	1, 6, 14	R: 90°
Mrk 463E	85	...	185	76	..., 4, 17	...

NOTES.—Cols. (2) and (3): Orientation of the outer galaxy isophotes in the IR (*J* band) and optical. Cols. (4) and (5): P.A. for the [O III] and radio emissions. An asterisk means that the orientation for the Hα + [N II] $\lambda\lambda$ 6548, 6583 is given. Col. (6): References. Col. (7): Structures (and their orientations) seen in the near-IR model-divided images. R = central red structure; B = stellar bar or disk; E = structure in emission.

REFERENCES.—Optical data: (1) Mulchaey et al. 1996; (2) Pogge & DeRobertis 1995; (3) Baldwin et al. 1987; (4) Schmitt & Kinney 1996; (5) Wilson et al. 1985; (6) Mulchaey & Wilson 1995; (7) Colbert et al. 1996; (8) Buta 1990; (9) Pedlar et al. 1992; (10) MacKenty 1990; (11) Pogge 1988; (12) Simpson et al. 1996. Radio data: (13) Neff & deBruyn 1983; (14) Wilson & Tsvetanov 1994; (15) Ulvestad & Wilson 1984b; (16) Cooke et al. 1998; (17) Ulvestad & Wilson 1984a.

(González-Delgado & Pérez 1996). The high excitation gas forms a V-shaped morphology to the southeast of the nucleus (in P.A. $\simeq 120°$ and extending for 8″) with a weaker northwest extension. The P.A. values of the [O III] λ5007 and Hα emissions are 112° and 107° (Mulchaey et al. 1996), respectively, in good agreement with the direction of the stellar bar. The P.A. values of the 3″ isophotes in *J*, *H*, and *K* band are 102°–114°, orientations similar to those of the bar and possible cone.

3.5.9. *NGC 4388*

NGC 4388 is a highly inclined ($i \simeq 72°$) Seyfert 2 galaxy that shows substantial dust obscuration. This galaxy displays a complex morphology in emission-line images (Pogge 1988; Corbin, Baldwin, & Wilson 1988). The Hα + [N II] image highlights H II regions in the disk of the galaxy. The [O III] λ5007 image, however, shows a conical shape along P.A. = 35° extending approximately 40″ (3.3 kpc) northeast and 20″ (1.6 kpc) southwest of the nucleus. Pogge (1988) argues that the [O III] λ5007–emitting gas is likely to be either photoionized by a nuclear continuum or shock ionized.

On large scales, our *J*- and *K*-band model-divided images clearly trace the H II regions in the spiral arms of this galaxy (positive residuals in Fig. 10 [Pl. 8]). In addition, another two structures outlined by positive residuals can be seen, the first extending at least 16″ (1.3 kpc) along P.A. $\simeq 45°$, and the second approximately 12″ (1 kpc) along P.A. $\simeq 228°$.

3.5.10. *NGC 5252*

NGC 5252 is a S0 galaxy classified as a Seyfert 1.5–1.9, with a large-scale ionization bicone (Tadhunter & Tsvetanov 1989). The overall galaxy orientation is at P.A. = 15° both in the near-IR (see Fig. 4*k*) and in the optical (Prieto & Freudling 1996). The *J*- and *K*-band model-divided images (not shown here) clearly trace the stellar disk at this position angle. The innermost regions of the model-divided images reveal the presence of a linear structure (also seen in the $J-K$ color map, not shown here) elongated in the east-west direction and unresolved in the north-south direction with an extension $\simeq 3''$ (2 kpc). Kotilainen & Prieto (1995) found a similar structure in their near-IR to optical color maps. Although the red linear feature seen in the NGC 5252 color map is real, we believe it is not a result of actual structure in the galaxy but rather reflects the combination of the high axial ratio of the stellar distribution and the presence of a bright unresolved nuclear source at *K*. The nuclear source (which is presumably transmitted radiation from the Seyfert 1 nucleus) contributes $\sim 35\%$ of the peak flux at *K* and therefore produces a much redder $J-K$ color at the nucleus. Along the major axis of the galaxy, the surface brightness of the stellar component drops slowly, and so the red nucleus has little effect on the overall color beyond the seeing disk. Along the minor axis, however, the stellar surface brightness decreases much more rapidly, so the nucleus has an effect on the color over a greater distance, which thereby produces an elongated feature in the color map. This interpretation is consistent with the fact that this feature is more closely aligned perpendicular to the major axis of the galaxy than to the ionization cone. In addition, scaling the *J* image to match the *K* image in a circumnuclear annulus, and then subtracting it, reveals only a nuclear point source, and no east-west structure.

4. DISCUSSION

In general we do not find any clear trend between the orientation of the EELRs and that of the IR continuum structures near the center of the galaxies. However, we do find bars or "bars within bars" in five of the 12 galaxies studied here, with two galaxies (NGC 2992 and NGC 4388) too inclined to detect a bar. It has been argued that bars might be responsible for transporting gas to the nuclei of galaxies. Codes modeling the gas flow in and around bars (see Athanassoula 1994 for a review) show that both the axial ratio and the strength of the bar influence the form of the shock loci: weak bars have curved shock fronts, with their concave part toward the bar major axis, while strong bars produce straight fronts. As noted by Athanassoula (1994) it appears that the most promising mechanism for pushing gas to the center of the galaxy is that of "bars within bars." The numerical simulations of the formation of double bars in galaxies carried out by Friedli & Martinet (1993) show that it is possible to form two bars simultaneously, together with a gaseous ring and eventual dissolution of the inner bar, or the formation of a large-scale bar first and then a second bar, and ultimately dissolution of the two bars. In both cases, an increase of the gas mass within the inner 0.2–1 kpc is predicted, with the gas being compressed into a region 10%–20% of the bar length. Further, the gas is expected to settle into a disk with rotation axis along the bar (see, e.g., Durisen et al. 1983). This disk could then collimate both the radio ejecta and the ionizing photons along the bar (Morris et al. 1985). If these predictions are correct, we might expect to see an alignment between the inner bar and the EELRs. The inner bars in NGC 1068, NGC 3081, and NGC 4253 are approximately aligned with their EELRs, which seems to support this scenario. Mrk 573 and NGC 3393 show evidence for double bars, but the orientation of their EELRs seems unrelated to their directions.

Finally, by inspecting Table 4, columns (7)–(9) and Table 5, column (4), we can explore the possibility of an alignment between the emission-line gas and the IR continuum on small scales. As mentioned above, such an alignment has been found in the optical (Mulchaey & Wilson 1995) for a sample of Seyfert galaxies of early types with well-defined emission-line axes and has been explained as possibly being due to the presence of an extended featureless continuum. Assuming that the typical errors in the determination of the P.A. of the [O III] λ5007 line emission are 10° (Mulchaey & Wilson 1995), we find that there is alignment between the line emission and the near-IR continuum in four galaxies—NGC 1068, NGC 2110, NGC 3081 and NGC 4253; of these, only NGC 2110 does not contain a bar. The alignment found in the near-IR for some galaxies could, in principle, contradict Mulchaey & Wilson's (1995) interpretation because any such a featureless continuum would be swamped by starlight in the near-IR. Among those galaxies with a near-IR alignment, two of them (NGC 2110 and NGC 4253) are in common with Mulchaey & Wilson (1995). Note, however, that NGC 5252 has a similar major axis P.A. in optical and near-IR continua but that these directions are not aligned with the line emission. Although it is not possible to derive any general conclusions from our small sample of Seyfert galaxies with EELRs, it appears that nonaxisymmetric structures may be playing some role in transporting material into the central regions. However,

there is no clear relationship between the orientations of bars and EELRs.

5. CONCLUSIONS

We have carried out a near-IR imaging study of a sample of type 1.5–2 Seyfert galaxies with EELRs, including some of the best studied examples of their class. The good observing conditions together with the small pixel size used have allowed us to obtain high-quality images, which have been analyzed in detail in order to gain insight into the structure of the inner and circumnuclear regions of the galaxies. In addition to standard synthetic aperture photometry (i.e., performed with fixed apertures in arcseconds), we have also obtained the near-IR colors of regions with linear diameters of 0.5 and 1 kpc, along with an annulus between these sizes. Previous studies of the near-IR properties of Seyfert galaxies have shown that the $J-H$, $H-K$, and $K-L'$ central colors (i.e., in a 0.5 kpc diameter aperture) are well explained by a mixture of an evolved stellar population plus a component of hot dust in emission. Here we propose a more realistic model (in view of the dusty torus scenario) in which the nonstellar source (hot dust with temperature $T \simeq 1200$ K) is significantly reddened ($A_V \approx 5-30$ mag), whereas the starlight is unreddened. There is little evidence from the $J-H$ and $H-K$ colors outside 0.5 kpc for emission from hot dust. However, the $K-L'$ circumnuclear (i.e., 0.5–1 kpc annulus) colors of some of the galaxies in our sample do show some indication of hot dust emission, although its contribution is smaller than in the nucleus. We argue that this extranuclear hot dust is heated by young stars.

The L'-band imaging has allowed us to quantify the extension of the emission at this wavelength, which shows both an unresolved and an extended component. We have also found that the unresolved source of the emission accounts for between 26% and 100% of the emission at L' band.

Finally, we have fitted elliptical isophotes to the near-IR images in order to produce smooth models of the stellar distribution. The model-divided images have been examined for isophotal deviations from elliptical symmetry, such as bars, spiral arms, and dust bands. The structures found in the model-divided images have been compared with the orientations of the EELRs, galaxy disk, and radio sources. We have found stellar bars in NGC 1068 and NGC 4253 and evidence for double bars (or "bars within bars") in Mrk 573, NGC 3081, and NGC 3393. The orientation of the inner bars of NGC 1068, NGC 3081, and NGC 4253 is approximately aligned with that of their EELRs, but in Mrk 573 and NGC 3393, the bars and the EELRs are not aligned (contrary to the conclusion of Axon & Robinson 1996). Our results suggest that there is no simple relationship between bars and EELRs.

We thank the anonymous referee for helpful comments. During the course of this work, A. A.-H. was partially supported by the National Aeronautics and Space Administration on grant NAG 5-3042 through the University of Arizona. C. S. was supported by NASA, through grants NAGW-3268 and HST GO-5411 from the Space Telescope Science Institute, which is operated by AURA, Inc., under NASA contract 5-26555, and by NATO through grant 675183. A. A.-H. would like to thank the Department of Astrophysics, University of Oxford, where part of this work was carried out, for their warm hospitality.

This work is based on observations collected at UKIRT. The United Kingdom Infrared Telescope is operated by the Joint Astronomy Centre on behalf of the U.K. Particle Physics and Astronomy Research Council. This research has made use of the NASA/IPAC Extragalactic Database (NED) which is operated by the Jet Propulsion Laboratory, California Institute of Technology, under contract with the National Aeronautics and Space Administration.

REFERENCES

Alonso-Herrero, A., Aragón-Salamanca, A., Zamorano, J., & Rego, M. 1996a, MNRAS, 278, 417
Alonso-Herrero, A., Ward, M. J., & Kotilainen, J. K. 1996b, MNRAS, 278, 902
Antonucci, R. 1993, ARA&A, 31, 473
Antonucci, R. R. J., & Miller, J. S. 1985, ApJ, 297, 621
Appleton, P. N., & Marcum, P. M. 1993, ApJ, 417, 90
Athanassoula, E. 1994, in Mass-Transfer Induced Activity in Galaxies, ed. I. Shlosman (Cambridge: Cambridge Univ. Press), 143
Axon, D. J., & Robinson, A. 1996, in Lecture Notes in Physics, 474, Barred Galaxies and Circumnuclear Activity, ed. Aa. Sandquist & P. O. Lindblad (Berlin: Springer), 223
Baldwin, J. A., Wilson, A. S., & Whittle, M. 1987, ApJ, 319, 84
Barvainis, R. 1987, ApJ, 320, 537
Boisson, C., & Durret, F. 1986, A&A, 168, 32
Buta, R. 1990, ApJ, 351, 62
Capetti, A., Axon, D. J., Macchetto, F., Sparks, W. B., & Boksenberg, A. 1996, ApJ, 469, 554
Colbert, E. J. M., Baum, S. A., Gallimore, J. F., O'Dea, C. P., Lehnert, M. D., Tsvetanov, Z. I., Mulchaey, J. S., & Caganoff, S. 1996, ApJS, 105, 75
Cooke, A. J., Baldwin, J. A., Ferland, G. J., Netzer, H., Wills, B. J., & Wilson, A. S. 1998, in preparation
Corbin, M. A., Baldwin, J. A., & Wilson, A. S. 1988, ApJ, 334, 584
Djorgovski, S., Weir, N., Matthews, K., & Graham, J. R. 1991, ApJ, 372, L67
Durisen, R. H., Tohline, J. E., Burns, J. H., & Dobrovolskis, D. R. 1983, ApJ, 264, 392
Elias, J. H., Frogel, J. A., Matthews, K., & Neugebauer, G. 1982, AJ, 87, 1029
Evans, I. N., Ford, H. C., Kinney, A. L., Antonucci, R. R. J., Armus, L., & Caganoff, S. 1991, ApJ, 369, L27
Evans, I. N., Tsvetanov, Z., Kriss, G. A., Ford, H. C., Caganoff, S., & Koratkar, A. P. 1993, ApJ, 417, 82
Fanelli, M. N., Collins, N., Bohlin, R. C., Neff, S. G., O'Connell, R. W., Roberts, M. S., Smith, A. M., & Stecher, T. P. 1997, AJ, 114, 575
Forbes, D. A., Ward, M. J., DePoy, D. L., Boisson, C., & Smith, M. S. 1992, MNRAS, 254, 509
Freedman, W. L., et al. 1994, Nature, 371, 757
Friedli, D., & Martinet, L. 1993, A&A, 277, 27
Friedli, D., Wozniak, H., Rieke, M., Martinet, L., & Bratschi, P. 1996, A&AS, 118, 461
Gavazzi, G., & Trinchieri, G. 1989, ApJ, 342, 718
Glass, I. S., & Moorwood, A. F. M. 1985, MNRAS, 214, 429
González-Delgado, R. M., & Pérez, E. 1996, MNRAS, 278, 737
Granato, G. L., & Danese, L. 1994, MNRAS, 268, 235
Haniff, C. A., Wilson, A. S., & Ward, M. J. 1988, ApJ, 334, 104
Helfer, T. T., & Blitz, L. 1995, ApJ, 450, 90
Hyland, A. R., & Allen, D. A. 1982, MNRAS, 199, 943
Kotilainen, J. K., Ward, M. J., Boisson, C., DePoy, D. L., Bryant, L. R., & Smith, M. G. 1992a, MNRAS, 256, 125
———. 1992b, MNRAS, 256, 149
Kotilainen, J. K., & Prieto, M. A. 1995, A&A, 295, 646
Krolik, J. H., & Begelman, M. C. 1988, ApJ, 329, 702
Lawrence, A. 1991, MNRAS, 252, 586
MacKenty, J. W. 1990, ApJS, 72, 231
Maiolino, R., & Rieke, G. H. 1995, ApJ, 454, 95
Maiolino, R., Ruiz, M., Rieke, G. H., & Papadopoulous, P. 1997, ApJ, 485, 552
Mazzarella, J. M., Voit, G. M., Soifer, B. T., Matthews, K., Graham, J. R., Armus, L., & Shupe, D. 1994, AJ, 107, 1274
McAlary, C. W., & Rieke, G. H. 1988, ApJ, 333, 1
McLeod, K. K., & Rieke, G. H. 1995, ApJ, 441, 96
Morris, S., Ward, M. J., Whittle, M., Wilson, A. S., & Taylor, K. 1985, MNRAS, 216, 193
Mulchaey, J. S., & Wilson, A. S. 1995, ApJ, 455, L17
Mulchaey, J. S., Wilson, A. S., Bower, G. A., Heckman, T. M., Krolik, J. H., & Miley, G. K. 1994, ApJ, 433, 625

Mulchaey, J. S., Wilson, A. S., & Tsvetanov, Z. I. 1996, ApJS, 102, 309
Neff, S. G., & deBruyn, A. G. 1983, A&A, 128, 318
Neugebauer, K., Oke, J. B., Becklin, E. E., & Matthews, K. 1979, ApJ, 230, 79
Oliva, E., Origlia, L., Kotilainen, J. K., & Moorwood, A. F. M. 1995, A&A, 301, 550
Origlia, L., Moorwood, A. F. M., & Oliva, E. 1993, A&A, 280, 536
Pedlar, A., Howley, P., Axon, D. J., & Unger, S. W. 1992, MNRAS, 259, 369
Peletier, R. F., & Balcells, M. 1997, New Astron., 1, 349
Pier, E. A., & Krolik, J. H. 1993, ApJ, 418, 673
Pogge, R. W. 1988, ApJ, 332, 702
———. 1989, ApJ, 345, 730
Pogge, R. W., & DeRobertis, M. M. 1993, ApJ, 404, 563
———. 1995, ApJ, 451, 585
Prieto, M. A., & Freudling, W. 1996, MNRAS, 279, 63
Rieke, G. H., & Lebofsky, M. J. 1985, ApJ, 288, 618
Sanders, D. B., Phinney, E. S., Neugebauer, G., Soifer, B. T., & Matthews, K. 1989, ApJ, 347, 29
Schmitt, H. R., & Kinney, A. L. 1996, ApJ, 463, 498
Simpson, C., Mulchaey, J. S., Wilson, A. S., Ward, M. J., & Alonso-Herrero, A. 1996, ApJ, 457, L19
Simpson, C., Ward, M. J., & Wilson, A. S. 1995, ApJ, 454, 683
Simpson, C., Wilson, A. S., Bower, G., Heckman, T. M., Krolik, J. H., & Miley, G. K. 1997, ApJ, 474, 121
Stone, J. L., Wilson, A. S., & Ward, M. J. 1988, ApJ, 330, 105
Storchi-Bergmann, T., Rodríguez-Ardila, A., Schmitt, H. R., Wilson, A. S., & Baldwin, J. A. 1996, ApJ, 472, 83
Tadhunter, C., & Tsvetanov, Z. I. 1989, Nature, 341, 422
Telesco, C. M., Becklin, E. E., Wynn-Williams, C. G., & Harper, D. A. 1984, ApJ, 282, 427
Thronson, H. A., Jr., et al. 1989, ApJ, 348, 158
Tran, H. D. 1995, ApJ, 440, 597
Tsvetanov, Z. I., Morse, J. A., Wilson, A. S., & Cecil, G. 1996, ApJ, 458, 172
Tsvetanov, Z. I., & Petrosian, A. R. 1995, ApJS, 101, 287
Turner, P. A., Forrest, W. J., Pipher, J. L., & Shure, M. A. 1992, ApJ, 393, 648
Ulvestad, J. S., & Wilson, A. S. 1984a, ApJ, 278, 544
———. 1984b, ApJ, 285, 439
Ward, M. J., Allen, D. A., Wilson, A. S., Smith, M. G., & Wright, A. E. 1982, MNRAS, 199, 953
Willner, S. P., Ward, M. J., Longmore, A., Lawrence, A., Fabbiano, G., & Elvis, M. 1984, PASP, 96, 143
Wilson, A. S., Baldwin, J. A., & Ulvestad, J. S. 1985, ApJ, 291, 627
Wilson, A. S., Braatz, J. A., Heckman, T. M., Krolik, J. H., & Miley, G. K. 1993, ApJ, 419, L61
Wilson, A. S., & Tsvetanov, Z. I. 1994, AJ, 107, 1227
Wozniak, H., Friedli, D., Martinet, L., Martin, P., & Bratschi, P. 1995, A&AS, 111, 115
Zhou, S., Wynn-Williams, C. G., & Sanders, D. B. 1993, ApJ, 409, 149